10. Large-Acceptance Multi-Particle Spectrometer SAMURAI

(**S**uperconducting **A**nalyzer for **Mu**lti-particle from **Ra**dio **I**sotope Beams)

Abstract

We propose to construct a large-acceptance multi-particle spectrometer for radioactive-beam experiments. The central part of the spectrometer system is a large-gap superconducting magnet with 7 Tm of bending power for momentum analysis of heavy projectile fragments and projectile-rapidity protons with large angular and momentum acceptance. The large gap also enables measurements of projectile-rapidity neutrons with large angular acceptance in coincidence with heavy projectile fragments.

This system is suitable for various radioactive-beam experiments such as electromagnetic dissociation including radiative-capture reactions, various direct reactions as well as polarized-deuteron-induced reactions and EOS studies.

List of Collaborators

Contact person:

T. Kobayashi (Tohoku Univ.)

Collaborators:

K. Summerer (*GSI*)

T. Murakami (*Kyoto Univ*.)

T. Teranishi (*Kyushu Univ*.)

A. Tamii (*Osaka Univ*.)

J. Murata (*Rikkyo Universit*y)

N. Aoi, S. Bishop, N.Fukuda, T. Gomi, T. Ichihara, K. Ikegami, T. Kubo, K. Kusaka, T. Motobayashi, J. Ohnishi, T. Ohnishi, H. Okuno, H. Otsu, K. Sekiguchi, N. Sakamoto, S. Takeuchi, K. Yoneda, Y. Yano (*RIKEN*)

T. Nakamura , Y. Satou (*Tokyo Inst. of Technology*)

T. Kawabata, Y. Maeda, K. Suda, H. Sakai, T. Uesaka, K. Yako (*Univ. of Tokyo*)

S. Kubono (*CNS, Univ. of Tokyo*)

T. Kajino (*NAO, Univ. of Tokyo*)

N. Chiga, N. Iwasa, H. Okamura (*Tohoku Univ*.)

[1] Introduction and overview

[1-1] Physics subjects to be investigated and observables to be measured

The large-acceptance multi-particle spectrometer is primarily designed for kinematically complete measurements by detecting multiple particles in coincidence, such as the invariant-mass measurement. The large bending power and large gap also enable various types of measurements. The following table summarizes the physics subjects in terms of the reaction types.

Reaction types	Category	Physics subjects	Observables
Electromagnetic dissociation (photon target)	Soft dipole excitation Giant resonance Radiative capture reaction	Single-particle orbit Collective motion Nuclear astrophysics	Invariant mass
Proton and light target	Elastic/inelastic, (p,p), (p,p') Knockout, (p,pN)	Density distribution Single-particle orbit	Missing energy & decay tagging
Polarized d beam Induced reaction	(d,d) (d,p)	2-3 nucleon force Short range correlation	polarization
4π measurement		Equation Of State	pions

(1) Soft Dipole Excitation via Coulomb Dissociation

Electromagnetic excitation by low-energy virtual photons induces direct non-resonant type excitations to continuum for neutron-rich nuclei with loosely-bound neutrons. The low-energy E1 strength can be studied utilizing invariant-mass spectroscopy by measuring the four-momenta of the outgoing heavy fragment and few neutrons in coincidence, as schematically shown in Fig.1.1. Such strength provides useful information on the ground state properties such as characteristics of the single-particle orbit. Measurements performed for 1-n halo nuclei ^{11}Be[1] and ^{19}C[2] give valuable information on the extended s-wave component of the single-particle state in light-mass region. In the new facility, measurements can be extended to N=21 and N=51 nuclei, where the lowering of 2p and 3s states are expected. In addition to the nuclear structure problems, it might be possible to extract information on the 2n correlations for neutron-rich nuclei with two weakly-bound neutrons [3].

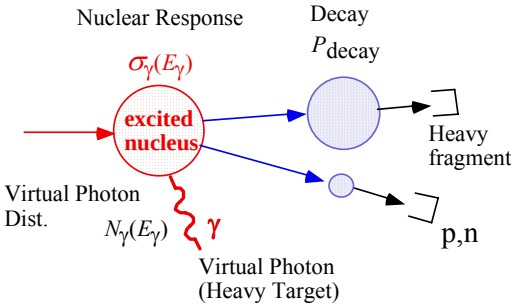

Fig. 1-1 : Electromagnetic dissociation via invariant-mass method

Electromagnetic excitation also provides an experimental tool to observe soft dipole resonance (SDR) related to the thick neutron skin with collective nature. Although this type of resonance has never been observed in the light-mass region, measurements extended into the heavier-mass region might give information on the collective motion in a very asymmetric system.

(2) Radiative Capture Cross Sections via Coulomb Dissociation

Radiative capture cross sections, $\sigma(p,\gamma)$, at low energies are of crucial importance for studying nuclear astrophysics. Electromagnetic excitation of proton-rich nuclei can be used to measure these cross sections utilizing the invariant-mass method and the principle of detailed balance.

Several reactions for the p-p chain and CNO cycle have been studied using the Coulomb dissociation method, for example, the $^{13}N(p,\gamma)^{14}O$ reaction which is a key reaction of hot-CNO cycle [4]; $^{7}Be(p,\gamma)^{8}B$ reaction related to the solar neutrino problem [5]; $^{22}Mg(p,\gamma)^{23}Al$ reaction relevant to break out of the NeNa cycle [6]; $^{8}B(p,\gamma)^{9}C$, $^{11}C(p,\gamma)^{12}N$ and $^{12}N(p,\gamma)^{13}O$ reactions relevant to hot p-p chain [7]. Using the Big-RIPS and a large-acceptance spectrometer, the cross sections for radiative capture reactions for explosive nucleosynthesis (the rp-, r-, and s- processes) in nova, supernova, X-ray bursts, etc., are expected to be measured. From these measured cross sections, more-reliable network-calculations on the nucleosynthesis can be expected.

Coulomb dissociation of proton-rich nuclei also provides experimental tool to study their nuclear structure, such as the occurrence of new magic numbers, near the proton drip line by observing the excited states.

(3) Direct nuclear reactions on a proton target

Direct reactions on the proton target, such as the proton elastic and inelastic scattering, (p,p) and (p,p'), and nucleon knockout reactions, (p,2p) and (p,pn), provide information on the nuclear density distribution of the whole system, spatial distribution of bound nucleons via momentum-distribution measurement, and single-particle orbit. Although the main part of these measurements is missing-energy measurement by detecting recoil nucleon(s), tagging the projectile fragment by the spectrometer allows studying the decay mode of the residual nuclei at the same time.

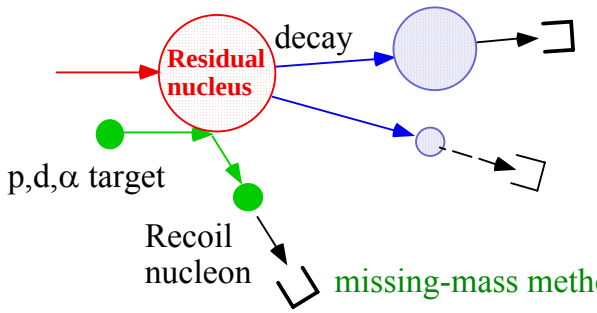

Fig. 1-2 : Tagging the decay mode of the residual nucleus after the direct reaction

(4) Two- and Three-nucleon interactions

One of the primary goals of nuclear many-body physics is to understand nuclear structure starting from the fundamental nucleon-nucleon (NN) interactions. The state-of-the-art NN interaction models, such as CD-Bonn, Nijmegen-I, AV18, can reproduce deuteron static properties and several thousands of NN scattering data almost perfectly. However, when the interactions are applied to nuclear structure calculations, it is revealed that the interactions alone cannot give the correct values of binding energies. Apparently, it is necessary to refine our understanding of the NN interactions to achieve the primary goal.

The purpose of this project is to improve our understandings of the nuclear interaction through polarization measurements with a primary beam of polarized deuterons with an energy of E_d < 880 MeV. The proposed investigations are:

- Three nucleon force effects in d+p scatterings [8], putting special focus on spin-dependences and relativistic effects.
- Short-range part of the NN tensor interactions probed by the polarization correlation measurements for the ^{3}He(d,p)^{4}He reaction [9].

(5) Asymmetry Energy of Nuclear Matter

RI beams provide a great opportunity to explore experimental constraints on the density dependence of the asymmetry energy of the nuclear equation of state (EOS). Although symmetry energy of the EOS has been well investigated through compressional giant resonances and collective flows observed in heavy ion collisions at intermediate and relativistic energies, the knowledge of asymmetric energy is still very limited.

Suggested by the recent theoretical calculations[10], we propose to measure the isospin dependence of π^+ and π^- production using a time projection chamber (TPC) installed in the large magnet gap for information on the density dependence of the asymmetry term at above normal densities.

[1-2] Requirements of the detector system

Mass Region

Measurements will be performed using RI beams up to A = 100, mainly limited by the availability of fully-stripped beams, and in the energy region between 250 – 300 MeV/A. This limitation comes mainly from the lack of the redundancy on the particle identification (PID) in the large acceptance spectrometer.

Particle identification

It is essential to identify mass and charge of the projectile fragment produced in the reaction. PID requires three independent measurements, such as charge (z), momentum (magnetic rigidity R), and velocity (β), or z, R, and total energy E. If 5 sigma mass separation ($\sigma_A = 0.2$) is required for

$A = 100$, error propagation, $\frac{\sigma_A}{A} = \sqrt{\left(\frac{\sigma_R}{R}\right)^2 + \left(\frac{\sigma_z}{z}\right)^2 + \left(\gamma^2 \frac{\sigma_\beta}{\beta}\right)^2}$ requires a rigidity resolution of $\frac{\sigma_R}{R} \approx \frac{1}{700}$ at $R \approx 2.2 GeV/c$, and a velocity resolution of $\frac{\sigma_\beta}{\beta} \approx 9 \times 10^{-4}$ at $\beta = 0.62 \sim 0.66$. The latter corresponds to timing resolution of $\sigma_T \approx 50 psec$ for 10 meters of flight path, which is marginal using our current technology. Obtaining a rigidity resolution of 1/1000 requires a combination of high-field magnet and precise position-measuring detectors. The required rigidity resolution for invariant-mass measurements is smaller than that required by PID.

Momentum resolution for polarized deuteron beam experiment

The required momentum resolution for 880 MeV deuteron is 1/1600 for good background suppression. The solid angle required is $\Delta\Omega \sim 6$ msr. In addition, well-shielded beam dump is necessary.

(γ,n)-type invariant-mass measurement

The dipole magnet is used as a sweeper for neutron measurement. The angular acceptance for neutrons, in a realistic setup, is ±5° vertically limited by the dipole gap, ±10° horizontally limited by the detector size. Detection efficiency for single neutron is about 70%. Relative-energy resolution is 0.5 MeV at 3-MeV decay energy.

(γ,p)-type invariant-mass measurement

Detection of heavy fragment and protons requires wide momentum acceptance of $R_{max}/R_{min} \approx 2 \sim 3$.

Summary of required measurements is shown in Fig. 1-3.

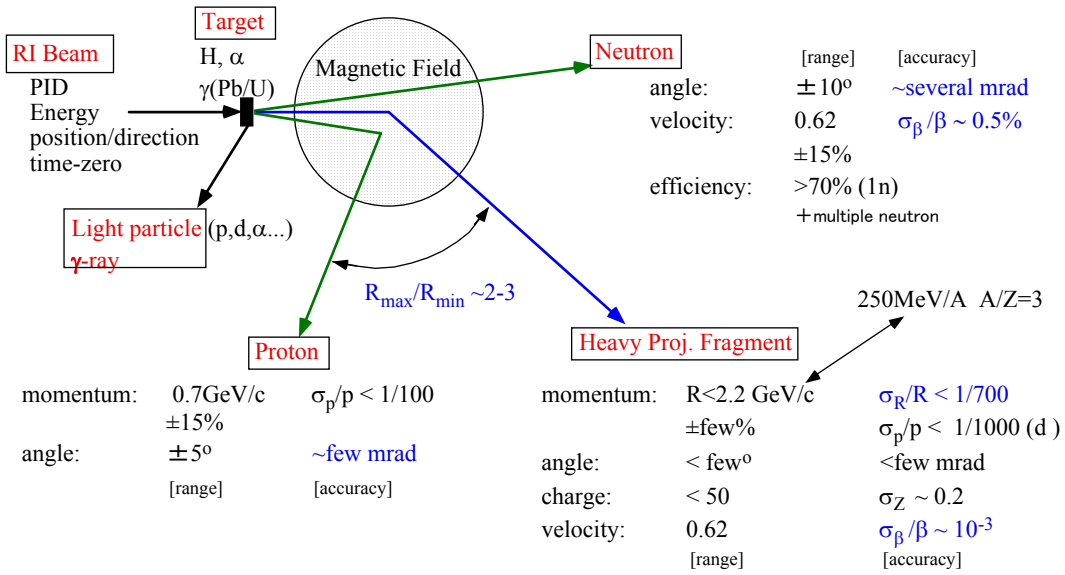

Fig. 1-3 : Summary of required measurements

[1-3] Detector system overview

Overview of the detector system for (γ,n)-type reaction is shown in Fig. 1-4a and Fig. 1-4b.

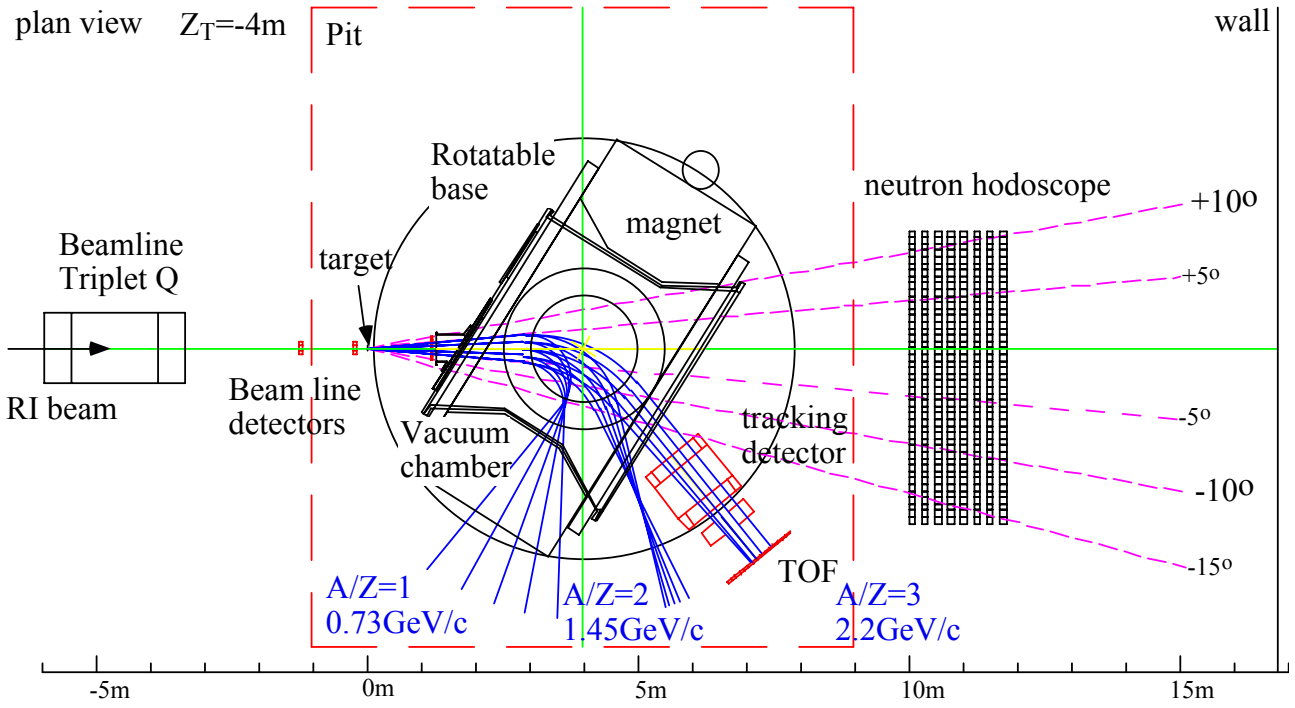

Fig. 1-4a : Overview of the detector configuration (top view)

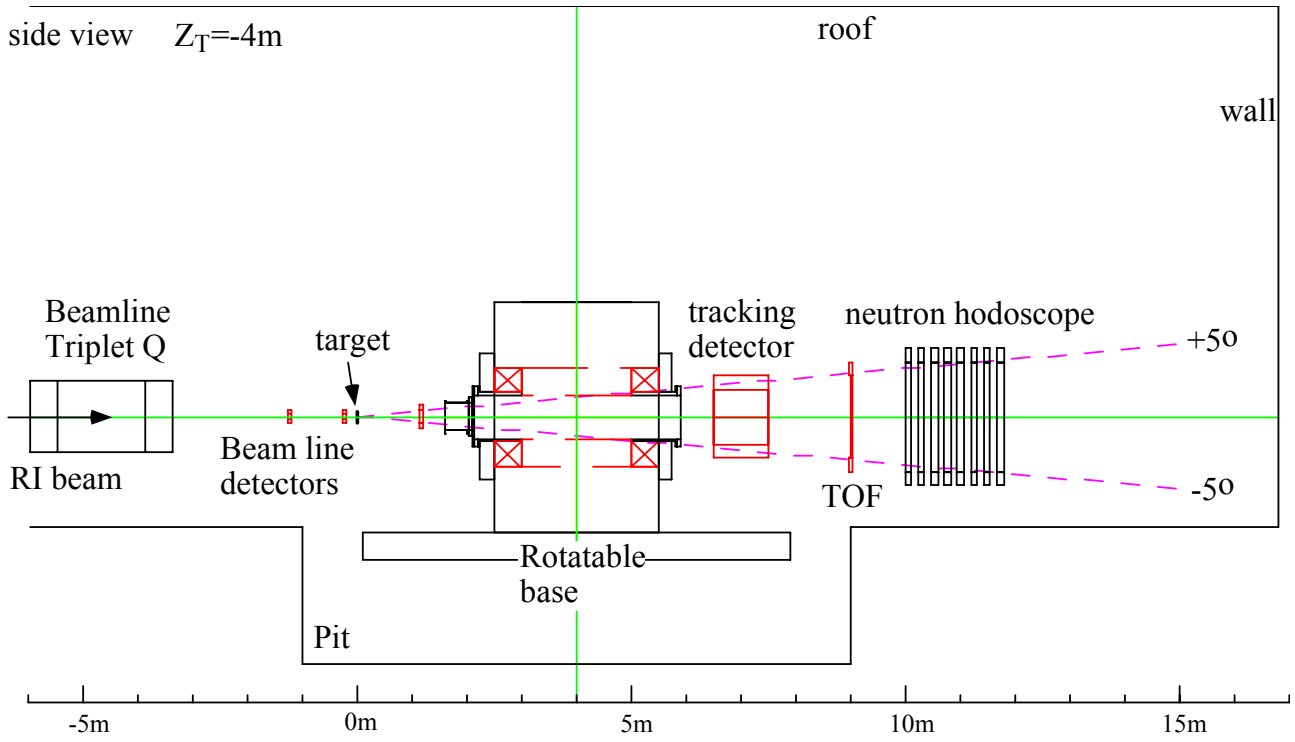

Fig. 1-4b : Overview of the detector configuration (side view) .

Detector configuration can be modified to fit various measurements as schematically shown in Fig. 1-5.

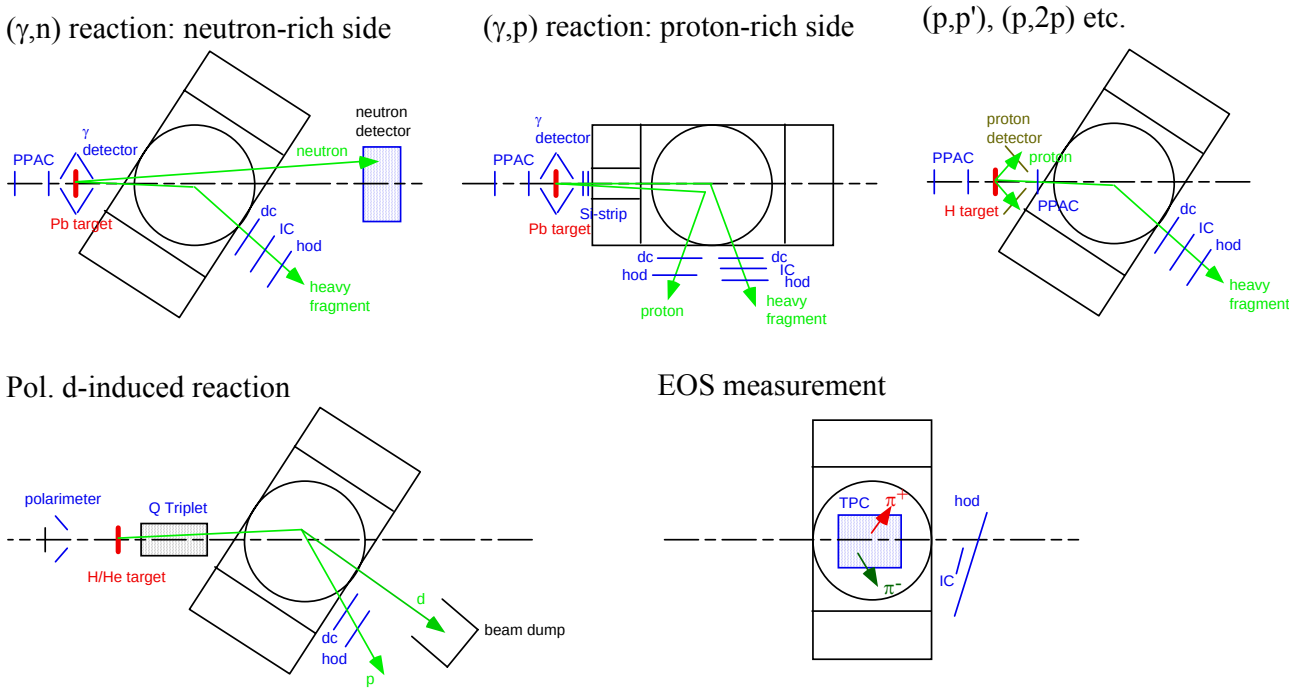

Fig. 1-5 : Experimental setup for various configurations

[1] T. Nakamura et al., Phys.Lett.B 331 (1994) 296; N. Fukuda et al., Phys.Rev. C 70 (2004) 054606.

[2] T. Nakamura et al., Phys. Rev. Lett. 83 (1999) 1112.

[3] S. Shimoura et al., Phys. Lett. B 348 (1995) 29.

[4] T. Motobayashi et al., Phys. Lett. B 264(1991) 259.

[5] T. Motobayashi et al., Phys. Rev. Lett. 73 (1994) 2680; N. Iwasa et al., J. Phys. Soc. Japan 65 (1996) 1256; T. Kikuchi et al., Phys. Lett. B 391 (1997) 261; T. Kikuchi et al., Eur. Phys. J. A 3, 213 (1998); N. Iwasa et al., Phys. Rev. Lett. 83, 2910 (1999); F. Schümann et al., Phys. Rev. Lett. 90, 232501 (2003).

[6] T. Gomi et al., Nucl. Phys. A734, E77 (2004).

[7] T. Minemura et al., *Symposium on Exotic Nuclei and Atomic Masses (ENAM2001)*, P183 (2002).

[8] N. Sakamoto et al., Phys. Lett. B 367 (1996) 60.; H. Sakai et al., Phys. Rev. Lett. 84 (2000) 5288.; K. Sekiguchi et al., Phys. Rev. C 65 (2002) 034003.; K. Sekiguchi et al., Phys. Rev. C 70 (2004) 014001; K. Sekiguchi et al., Phys. Rev. Lett 95 (2005) 162301.

[9] T. Uesaka et al., Phys. Lett B 467 (1999) 199.; T. Uesaka et al., Phys. Lett. B 533 (2002) 1.

[10] Bao-An Li, Phys. Rev. Lett. 88, 192701 (2002); Nucl. Phys. A708, 365 (2002).

[11] G. Rai, et al., IEEE Trans. Nucl. Sci. 37, 56 (1990).

[12] H. Herndl et al., Phys. Rev. C52, 1078 (1995); P. G. Thirolf et al.,, Phys.Lett. B 485, 16 (2000).

[2] Detector Systems

[2-1] Spectrometer magnet

Design policy

A large-gap superconducting dipole magnet is a central part of the detector system. The following list contains the requirements on the dipole magnet.

From the experimental side:

- Large field integral: for high precision momentum analysis.
- Large magnet gap: for large vertical acceptance for neutrons.
- No coil link: for large acceptance in the horizontal direction
- Small fringing field: for detectors around the target region and tracking detectors.
- Flexibility for various experimental configurations
- Large momentum acceptance: for heavy fragments and protons in coincidence
- High momentum resolution: for deuteron-induced reactions

From magnet construction:

- Simple structure: H-type magnet, round coil
- Cryostat structure similar to SRC: proved technology
- Utilize available superconductor: to reduce cost

Superconducting magnet

Out of various designs, following parameters are selected:

- H-type superconducting magnet with a round pole, because of the simple structure
- Field integral of 7 Tm, providing rigidity resolution of 1/700 (rms) at 2.3 GeV/c , and particle identification up to A = 100.
- Vertical gap of 80 cm, providing vertical angular acceptance of ±5 degrees for projectile-rapidity neutrons.
- Rotatable base from 0 to 180 degrees, for various experimental configurations
- Field clamp, to minimize the fringing field
- Built-in vacuum chamber with flanges, for effective usage of the magnet gap.
- Holes in the return yoke, for detecting projectile rapidity protons and heavy fragments in coincidence with R_{max}/R_{min}=2-3.
- Q3D option for high-resolution measurement, last triplet Q magnet in the beam line is used with the dipole magnet in the Q3D mode, providing momentum resolution of 1/3000.

Magnetic parameters are summarized as follows:

- Maximum magnetic field: 3 T @ 3.6 MAT
- Maximum field integral: 7 Tm
- Stored energy: 28 MJ
- Expansion force: 200 tonne/m (self support possible)

- Vertical force: 650 tonne (coil link not necessary)

The magnet is shown in Fig. 2-1-1. Total weight is 650 tonne.

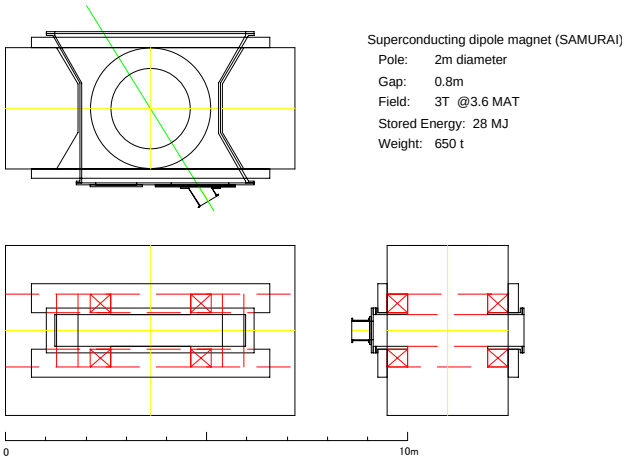

Fig. 2-1-1: Drawing of the superconducting dipole magnet

Magnetic field

The fringing field is minimized by changing the thicknesses of the return yoke and the field cramp. Although not fully optimized yet, the return yoke thickness and the field clamp are chosen as 1.8 m and 0.25m, respectively. The magnetic field distribution in the mid plane at 3 T is shown in Fig. 2-1-2, with and without field clamp. As clearly shown, the fringing field beyond 2.0 m from the center, where tracking detectors are placed, is less than 50 Gauss with the field clamp.

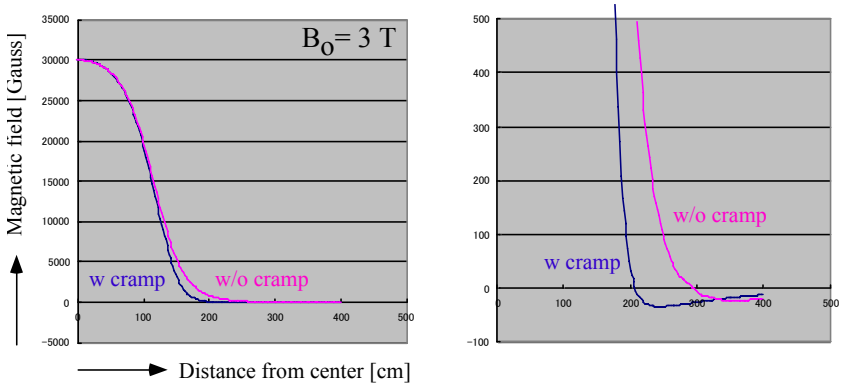

Fig. 2-1-2 : Magnetic field distribution in the mid plane

Superconductor, main coil structure, and helium cryogenic system

The superconductor and main coil structure are being designed by a team in the RIKEN accelerator facility under tight communication with experimental groups. The team has accumulated a lot of techniques and know-how through the design and construction of the superconducting cyclotron, and has sufficient potential for designing the magnet. The team offered a number of choices of the superconductor and coil structure, and careful selection is being made so that they match the scale of the magnet. As for the cryogenic system, the team proposed that the SAMURAI magnet equips a helium system separate from the

ones for accelerators, and it is also being designed. Utilizing existing techniques is effective in reducing costs and man power for development.

Cost estimate and man power

The cost of the superconducting magnet, including the vacuum chamber, roratable base, and He cryogenic system, was estimated by 2-3 companies. The estimated cost is approximately 1,000 MYen and it still has large ambiguities.

The accelerator group of RIKEN accelerator facility, headed by Okuno, is responsible for the detailed design of the superconducting magnet.

[2-2] Detector system for heavy fragments

[2-2-1] Rigidity analysis and tracking detectors for heavy fragments

Detector configuration

The rigidity (momentum) resolution required for particle identification (PID) for $A=100$ is $\frac{\sigma_R}{R} \approx \frac{1}{700}$ at $R \approx 2.2 GeV/c$. Considering a typical setup as shown in Fig. 2-2-1, momentum is evaluated from target position information (x_T, y_T) provided by upstream beam detectors, and position (x_d, y_d) and angle (x'_d, y'_d) information by downstream detectors. Momentum resolution is roughly estimated based on the relation, $\left(\frac{\sigma_R}{R}\right)^2 = \left(\frac{(\theta|\theta)}{D_{eff}}\sigma(x_D)\right)^2 + \left(\frac{(x|\theta)}{D_{eff}}\sigma(x'_D)\right)^2 + \left(\frac{\sigma(x_T)}{D_{eff}}\right)^2$. Using typical matrix elements: $D=2.0\ cm/\%$, $D'=7.9\ mrad/\%$, $(x|\theta)=0.32\ cm/mrad$, $(\theta|\theta)=0.12$, $D_{eff}=(\theta|\theta)D-(x|\theta)D'=-2.3\ cm/\%$, the most important quantity is the angular resolution $\sigma(x'_D)$ of the downstream detectors. In order to have the required momentum resolution, an angular resolution of about $\sigma(x'_d) \approx 1\ mrad$ is necessary. This requires a low-mass chamber, much less than $L/L_R < 10^{-3}$, with a good position resolution. Optional measurement of angles in front of the magnet will improve the momentum resolution, but will sacrifice the capability of multiple-particle detection.

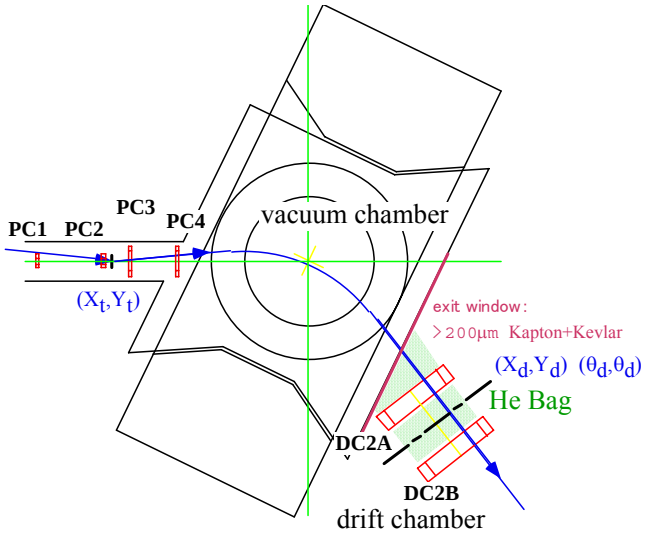

Fig. 2-1-1 : Momentum analysis (plan1)

When the downstream detectors are placed behind the large vacuum window (not designed yet, but the thickness is about 0.3 mm thick Kapton + Kevlar), the window will introduce $L/L_R \approx 10^{-3}$ of scattering material and secondary interaction.

Choice of downstream drift chamber : Low-pressure drift chamber

It is almost a unique solution to use drift chamber (DC) without field shaping as a downstream detector, considering the size of the detector and the incident angle of heavy fragments. In order for DC to operate properly for various fragments, i.e. from light to heavy fragments, it is important to control the gas gain and drift field independently. For that purpose, we consider operating the DC at low pressure, introducing the gas pressure as the second parameter in addition to the high voltage. Although not used commonly, a low-pressure DC has following advantages:

- two operational parameters to control gas gain and drift field independently,
- operation of DC in the vacuum chamber with relatively rarefied gas windows,
- angle and position measurements before the thick exit vacuum window.

Operation of gas detectors at low pressure has been studied for multi-wire proportional chamber (MWPC) with 2mm anode spacing, and a high-rate drift chamber with 2.5mm drift distance, using pure C_2H_6 or i-C_4H_{10} as detector gas. The low-pressure MWPC has HV plateau with 100% efficiency even for minimum ionizing particles (MIP, i.e. β-rays and cosmic μ), and works down to 30 torr for ^{40}Ar at 250 MeV/A. The high-rate DC is so far tested with cosmic μ: operation is stable down to 0.25 atm for MIP with a position resolution of $\sigma_x = 130\mu m$, which is slightly worse than that at 1 atm. Since both detectors use foil cathodes, the feedback effect due to ultraviolet light produced in the avalanche is less severe compared with the chamber with wire-cathode structure. Bench tests of a hexagonal drift chamber with a 13mm drift length shows that HV plateau has 100% efficiency for MIP down to 300 torr.

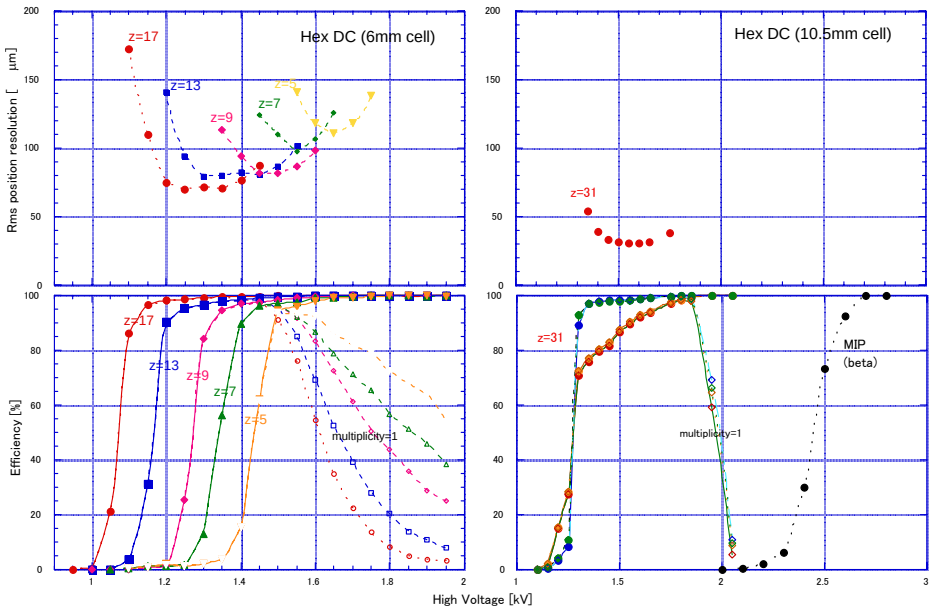

Fig. 2-1-2 : Measured HV dependencies of efficiency and resolution of Hex DC at 1 atm using He+50%C_2H_6

Prototype tests for downstream DC

Hexagonal cell structure (Hex DC) is chosen for downstream DC because

- electric field has rotational symmetry, suited for inclined tracks,

- hexagonal structure provides less detector material.

Prototypes, with 6 mm, 10.5 mm, and 13 mm drift distance, have been tested at 1 atm using He+50% C_2H_6 as filling gas. For He-based gas mixture, the radiation length is about 4 times longer compared with Ar-based gas. Bench tests using cosmic-ray μ show the position resolution is $\sigma_x = 110 - 150 \mu m$ for a C_2H_6 fraction of 60% to 20%.

The Hex DC has also been tested for heavy ion beams at 250-300 MeV/A and 1 atm. High voltage dependences of efficiency and position resolution are shown in Fig. 2-1-2A (6 mm cell, Z = 5 to Z = 17) and Fig. 2-1-2B (10.5 mm cell, Z = 31 and MIP). Position resolution is $\sigma = 110 \mu m$ for Z = 5, $\sigma = 70 \mu m$ for Z = 17, and $\sigma = 30 \mu m$ for Z = 31. Beam tests at low pressure using pure quenching gases, C_2H_6 and i-C_4H_{10} , are scheduled in December 2005.

During these tests, it turns out that path-length variation in the hexagonal cell causes a HV plateau shift by a significant amount depending on a position in one cell. We are planning to check a square cell structure as well, in order to find the optimum cell structure for the downstream DC.

Preliminary design of downstream DC

Although final design of the downstream DC requires more R&D, the preliminary design is as follows:

- hexagonal (or square) cell structure: for electric field with rotational symmetry and reduction of detector material,
- cell size : drift distance of (6-)10 mm,
- layer structure : xx'xx'xx'yy'yy'yy' with shield planes,
- size : 100cm horizontal width placed at 2.5 m from the magnet center, which corresponds to momentum acceptance of about ±15%. Vertical size of about 60 cm so that the detector fits in the vacuum chamber extension.
- low pressure operation in vacuum chamber

When a Hex DC structure is chosen with drift distance of 10mm, xx'xx'xx'yy'yy' configuration, 80 μmϕ Au-Al wire for field wires, 30 μmϕ Au-W/Re wire for anode wires, the detector thickness/chamber is $L/L_R \approx 0.35 \times 10^{-3}$ when C_2H_6 gas is used at 0.2 atm. The number of readout channels is 48ch/plane for X, and 32 ch/plane for Y. Separate HV is applied to shield planes so that all planes have the same gas gain. The number of readout channels/chamber is 480 ch/chamber. If a position resolution of 150 μm/plane can be achieved at low pressure, two chambers separated by 50 cm in vacuum will give an angular resolution much less than 1 mrad.

Downstream DC in vacuum chamber

Operation of large drift chambers in vacuum requires further technical developments, such as the mechanism for position adjustment, and cooling mechanism for ASD boards in low-pressure gas.

Digital readout electronics for downstream DC

We have developed compact 16ch ASD boards for drift chambers using custom IC chips (CXA3653 with 80 nsec decay time & CXA3183 with 16 nsec decay time), developed originally for the ATLAS muon

chamber. Compared with old-fashioned LRS2735DC, the overall gain is about 20, enabling the operation at very low threshold. High gain in the readout electronics also helps avoid the aging effect caused by high intensity beams. There is no problem to operate the chamber up to 0.5 MHz/cell for 6mm cell.

LVDS outputs from the ASD boards are sent to 64ch AMT-VME TDC modules via twisted-pair cables, and timed with 0.78 nsec/ch accuracy and multi-hit capability. A TDC module provides width encoding so that rough pulse height information can be obtained in addition to the drift time information.

Upstream position detectors

For some measurements, optional position detectors can be added between the target and spectrometer magnet in order to increase the momentum resolution. Due to the necessity to solve left-right ambiguity in the DC, a minimum of 6 planes are necessary for a two-dimensional measurement. As upstream position detectors, we have developed low-pressure cathode-readout drift chamber (LP-KDC) as thin position detectors. Position information is obtained by measuring the induced charge on the cathode strips. A prototype LP-KDC with active area of 100mm x 100mm has been constructed. The anode structure is Walenta-type DC with 5mm drift length and 5mm half gap. Cathode strip of 7 mm pitch is processed by laser on 4 μm-thick Al-nized polypropylene. Electrical contact between the strip and readout pad is made by conductive ink. Two-dimensional readout requires 5 planes arranged as, strip cathode (x), anode(y), cathode, anode(x), and strip cathode(y), and the total detector thickness is $L/L_R \approx 0.08 \times 10^{-3}$. Unlike PPACS, LP-KDC is MIP sensitive.

LP-KDC has been tested using cosmic rays, 250 MeV/A Ar beams, and 300 MeV/A Kr beams. A position resolution of $\sigma_x = 100 \mu m$ is obtained for the MIP using He+C_2H_6 at 1 atm, with relatively large angular dependence. For Ar beams, the best position resolution obtained is $\sigma_x = 170 \mu m$ using i-C_4H_{10} at 20 torr. Since analog readout electronics had some problems during the test, we hope the resolution can be improved. For Kr beams, HV dependence of resolution is shown in Fig. 2-1-3: the best resolution is $\sigma_x = 100 \mu m$ using i-C_4H_{10} at 20 torr. It is not clear at the moment why the position resolution is so bad.

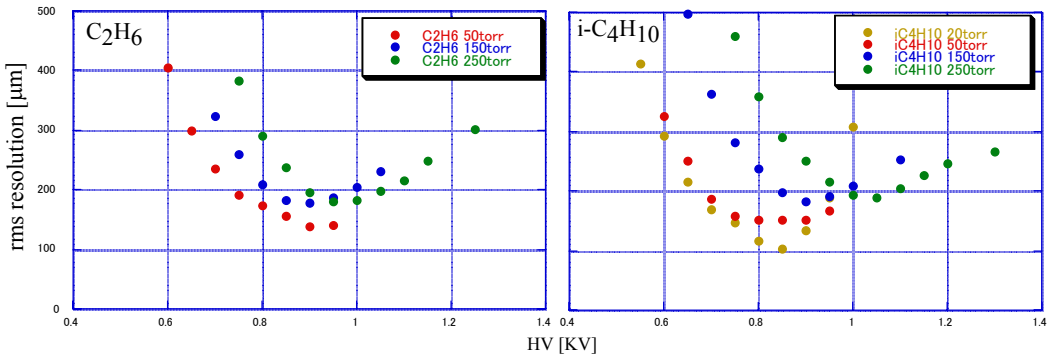

Fig. 2-1-3 : HV dependence of LP-KDC rms position resolution for 300 MeV/A Kr beams.

The same ASD board is used for analog readout of cathode strips with slight modifications. Since the time constant of the analog signal is 16 nsec and charge-integrating ADC is used, operation at high rate poses no major problems. The drawback of this system is the number of readout channels: 16 channels are

necessary for 100 mm active area in one direction. Remaining R&Ds required for LP-KDC are (1) establish the method to make bigger cathode strips, and (2) develop an active analog-delay module to avoid cable delays.

Preliminary design of upstream chambers

Preliminary design parameters of upstream chamber are as follows.

- two chambers with an effective area of 128 mm x 128 mm and 256 mm x 256 mm,
- plane configuration: window, shield, strip cathode (x), anode(y), cathode, anode(x), strip cathode (y), shield, and window,
- number of readout channels is 32 ch for the 1st chamber, and 64 ch for the 2nd chamber
- half gap of 6 mm and drift length of 6 mm,
- 20 μmϕ Au-W/Re for anode wires and 80 μmϕ Au-Al for potential wires,
- 8.5mm cathode strip pitch, made by Al-evaporation on 4 μm-thick Mylar foil,
- two chambers separated by 50 cm to get 0.4 mrad angular resolution assuming $\sigma_x = 150\mu m$, and allow $\pm 10^o$ opening for neutron detection,
- two more identical chambers with 128mm x 128mm active area to be used for beam tracking in front of the target.

Tracking detector configuration for heavy fragments

The configuration of tracking detectors for heavy fragments is shown schematically in Fig.2-1-4. The incident beam vector is measured by LP-KDC's, vector of heavy fragment is measured by upstream LP-KDC's before the magnet and by downstream DC's after the magnet. They are all operated at low pressure in the vacuum chamber.

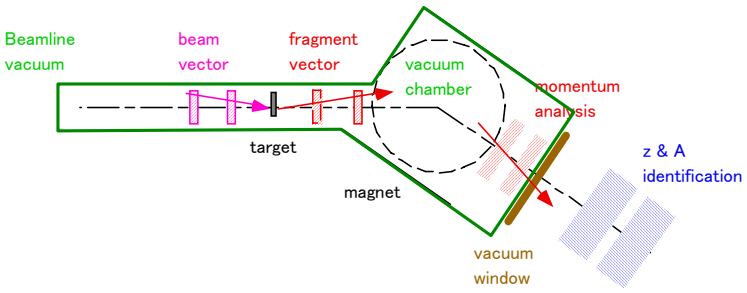

Fig. 2-1-4 : Schematic configuration of tracking detectors.

Cost estimate: unit in KYen

- Beam Chamber : Cathode readout drift chamber sub total: 7,080
  - chamber/case/feedthrough: 1,500 /chamber x 2 3,000
  - # readout channels (analog)= 16ch x 2
  - electronics: 20(ASD)+20(cables)+300(receiver/delay)+20(cable)+ 10(PS)+400(ADC)= 770 /16ch

770 /16ch x 4= 3,080

- low-pressure gas handling 1,000

• Upstream chamber: Cathode readout drift chamber sub total 9,620

- chamber/case 1,500(front)+2,500(back) 4,000
- #readout channels (analog) = 16ch x 6
- electronics: same as beam chamber, 770 /16ch x 6 4,620
- low-pressure gas handling 1,000

• Downstream chamber: Hexagnal drift chamber sub total 58,800

- chamber/case/feedthrough 25,000 /chamber x 2 50,000
- #readout channels (digital) = 16ch x 60 = 960 ch
- electronics: 20(ASD)+20(cables)+10(PS)+80(TDC)= 130 /16ch

  130 /16ch x 60= 7,800
- low pressure gas handling 1,000

Man power

Kobayashi, Chiga (staff, Tohoku) + 2-3 graduate students (Tohoku)

[2-2-2] Detectors for particle identification

Choice of detectors for particle identification

Particle identification of heavy fragments requires velocity measurement or total-energy measurement in addition to the rigidity and the charge measurement. In order to have 5σ separation ($\sigma_A = 0.2$) at A=100, velocity resolution of $\sigma_\beta / \beta = 9 \times 10^{-4}$ $@\beta = 0.6$ or total energy resolution of $\sigma_E / E = 2.5 \times 10^{-3}$ is necessary. When the TOF method is used for velocity measurement, necessary time resolution is $\sigma_T = 50 psec$ for 10 meters of flight path. Considering the necessity of a thin start detector for TOF, this method seems to be marginal.

We have considered two techniques for velocity and total-energy measurements: a Cherenkov detector operated at the total internal reflection (TIR Cherenkov) for velocity measurement and NaI(Tl) detector for total-energy measurement.

Total internal reflection (TIR) Cherenkov detector

Principle of the TIR Cherenkov detector is shown schematically in Fig. 2-2-1.

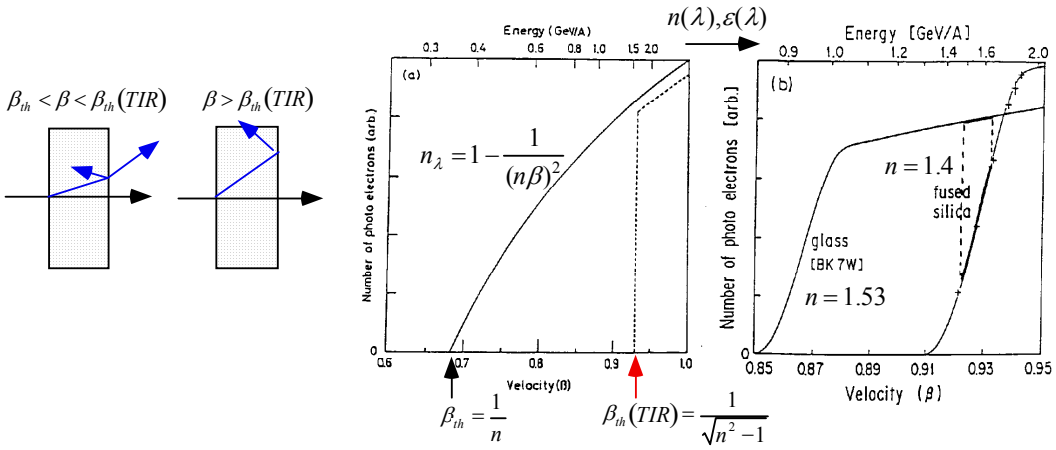

Fig. 2-2-1 : Principle of the TIR Cherenkov detector.

When particle velocity is higher than TIR threshold $\beta_{th}(TIR) = 1/\sqrt{n^2 - 1}$, all the Cherenkov light is transmitted to the end of radiator by total internal reflection. Therefore the light yield will show sharp rise at the TIR threshold. Although the slope becomes finite due to the wavelength dependence of index of reflection, it is still steep enough to measure the velocity in high precision by measuring the Cherenkov light yield. This method was once used in the HISS detector system to measure the mass around A=40 at 1.65 GeV/A with a mass resolution of $\sigma_A = 0.21$: the equivalent velocity resolution is $\sigma_\beta = 4 \times 10^{-4}$ $@\beta = 0.93$.

When this method is applied to 250-300 MeV/A energy regions, it is necessary to find a radiator with high index of reflection. Such material tends to have large dispersion, not suited for high precision measurement.

Prototype test of TIR Cherenkov

Out of various candidate materials, we choose TADF30 glass (n=1.92 @400nm) and transparent Ceramic (n= 2.08 @400nm) as radiators. They were tested using Ar beams and secondary beams from Kr beams between 150-350 MeV/A. Preliminary results for TAFD30 are shown in Fig. 2-2-2.

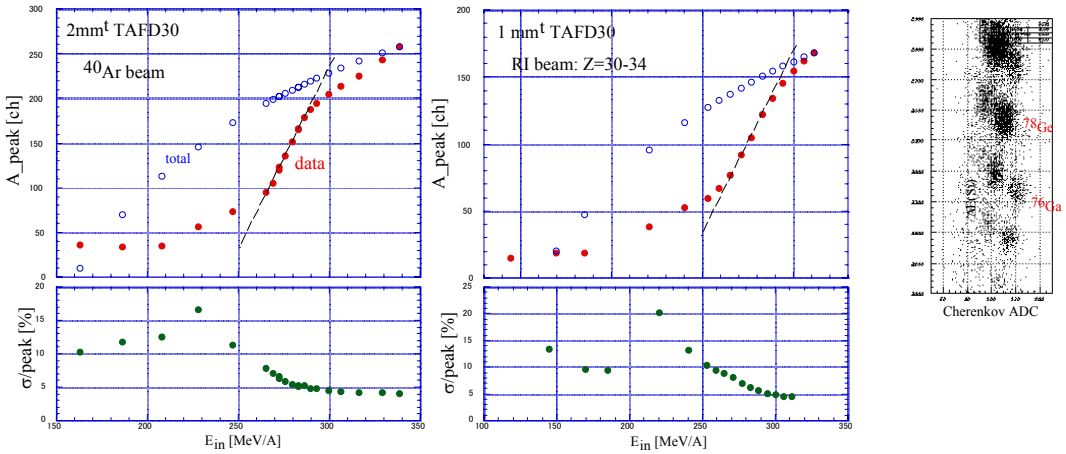

Fig. 2-2-2 : Pulse height of TIR Cherenkov for Z=18 (left) and Z=29-33 (center). PID by ΔE(Si) and Cherenkov at 280 MeV/ (right) for A~80.

In both cases, the Cherenkov light yield shows a steep rise between 260 MeV/A and 290 MeV/A as expected. Particle identification by ΔE measurement of 300 μm-thick Si and TIR Cherenkov is shown in the far right figure in the middle of steep slope: isotope separation for Z = 30, 31, 32 are clearly observed.

Although the mass resolution is worse compared with total-energy measurement using NaI(Tl) detectors, TIR Cherenkov detector will provide PID for A=80 at 280 MeV/A without stopping the fragment. In practice, it is not easy to make large-area Cherenkov hodoscope. Therefore the best place to put TIR Cherenkov detector is between the target and the magnetic spectrometer.

NaI(Tl) detector for total energy measurement

It is well known that PID by ΔE-E method alone is difficult for heavy fragments. We therefore consider to combine ΔE-E measurement with rigidity analysis by the magnetic spectrometer. The ΔE measurement will be done by Si detectors or an ion chamber, and E measurement by a NaI(Tl) detector.

Test of NaI(Tl) scintillator

Results of the first test of a 3"ϕx3" NaI(Tl) crystal for secondary beams from ^{40}Ar beams at 190 MeV/A are shown in Fig. 2-2-3. Helped by the momentum selection of ±0.5% at the momentum dispersive focal plane in the secondary beam line, isotopes are clearly separated by ΔE-E below Z = 17. The energy resolution is also checked for 290 MeV/A ^{40}Ar beams: $\sigma_E / E = 0.4\%$ when a charge integrating-type ADC is used.

In the next test using secondary beams from 400 MeV/A ^{84}Kr beams, the energy resolution of NaI(Tl) scintillator can be improved to $\sigma_E / E = 0.15\%$ for 290 MeV/A ^{78}Ge when a charge-integrating preamp

and shaping amplifier with 1μs shaping time are used. It is therefore no problem to separate mass around A = 80 at 290 MeV/A. Total energy distribution for Z = 32 is shown in Fig. 2-2-4: clear separation of ^{77}Ge and ^{78}Ge is shown.

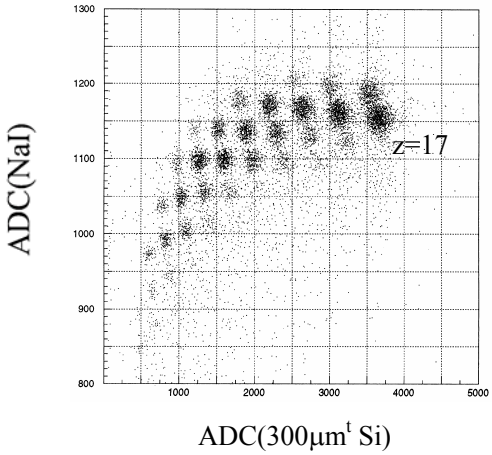

Fig. 2-2-3 : PID by ΔE(Si)-E(NaI) for fragments A<40 and Z<17 at 190 MeV/A

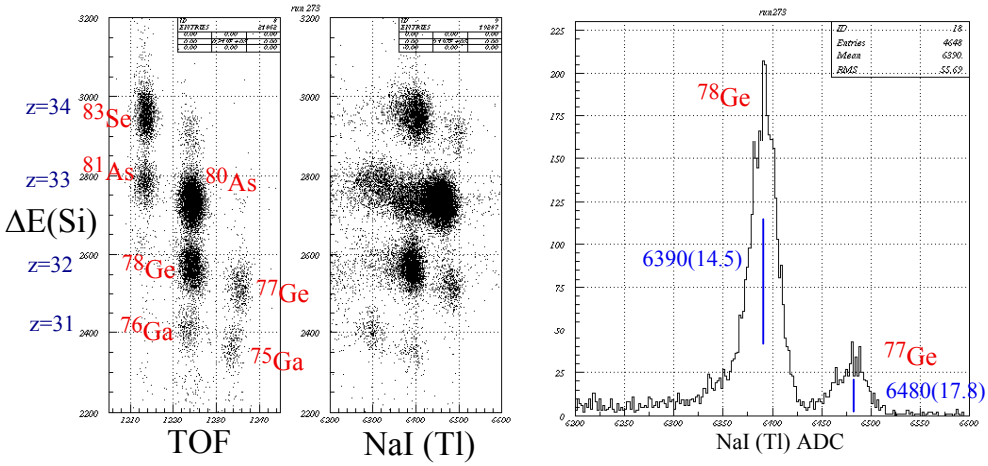

Fig. 2-2-4 : Total energy distribution for Z = 32 at 290 MeV/A

Also from these tests, a relatively-large position dependence is observed. The reason is not clear, but might be attributed to the non uniformity of doped Tl. There is one more problem for NaI(Tl): without optimizing the photomultiplier breeder, the HV has to be set to a very low voltage to avoid saturation of the signals, making the operation unstable sometimes.

Preliminary design of the total-energy measuring detector

In principle, NaI(Tl) gives us enough energy resolution to separate isotopes around A=80 at 300 MeV/A. The necessary size of the NaI(Tl) detector, placed about 8 meters from the target, seems to be determined by the angular spread of the secondary beam. Assuming ±15 mrad in angular spread, the necessary area is about 25 cm^2. In order to cover a larger area, one method is to stack modular NaI(Tl) crystals with cubic

shape; however, Al housing and MgO reflector might cause problems when fragments pass through two crystals. Another method is to use a large-area NaI(Tl) crystal similar to the one used in the Anger camera application. A planar NaI(Tl) crystal of 370mm x 370m x 25mm is available. With this, it is necessary to find a way to put photomultipliers with breeder design optimized for low-voltage operation. An anticipated problem with this system is the capability for high-rate beams.

It is also an interesting option to use CsI(Tl) crystals read out by photo diodes. Since CsI(l) can be used with a small amount of reflector materials, stacking modular CsI(Tl) crystals may cause less problems. It is also advantageous to use photo diode because the gains can be adjusted more reliably using charge-sensitive preamplifiers. We therefore plan to test CsI(Tl) crystals with PD readout using heavy beams in December 2005.

Ion Chamber for charge measurement

We plan to use a tilted electrode ion chamber (TEGIC) developed by K. Kimura described in NIM A538 (2005) 608. So far, an ion chamber with 200mmϕ cross section has been built.

For a moment, we need an ion chamber with 370 mm x 370 mm active area, whose acceptance is roughly the same as the downstream NaI(Tl) crystal. With this size, we can adopt the conventional construction method. Since high rate capability is limited by the NaI(Tl) detector, 30 mm gap can be used instead of 20mm in the original design. An ionization region of 48 cm can be read out by 8 anode planes to get enough charge resolution.

Cost estimate for PID detectors

*Detector for total-energy measurement: sub total : 7,000 KYen

method: 370mm x 370mm x 25mm NaI(Tl) with photomultipliers

detector cost: about 6,000 KYen

electronics: about 1,000 KYen(charge integrating PA + Shaping Amp + ADC)

*Detector for charge measurement : sub total : 4,360 KYen

method : ion chamber with 370mm x 370mm cross section
480mm deep read out by 8 anodes

detector cost: 3,000 KYen (including R&D)

electronics: 20 (PA) + 50(SA) + 100(ADC) = 170 KYen/ch
170 KYen/ch x 8= 1,360 KYen

Man power

Kobayashi, Chiga (Staff, Tohoku) + 2-3 graduate students

[2-3] NEBULA

(Neutron-detection system for Breakup of Unstable-Nuclei with Large Acceptance)

[2-3-1] Introduction

In invariant mass spectroscopy, we study **unbound states** above the neutron-decay threshold, which is of vital importance in the region of very-neutron rich nuclei where the RIBF is going to explore. One of the important physics subjects to be investigated is 1) "collectivity" at the very neutron-rich extremes such as giant resonance (soft dipole resonance, pigmy resonance) studied by the Coulomb and nuclear dissociation. In addition, the invariant mass spectroscopy will give a powerful tool for probing 2) the low-lying unbound states at very neutron rich nuclei, 3) unbound exotic states such as ^{10}He, '4n' system, $^{25\text{-}28}$O etc.

The neutron detector arrays are essential in the invariant mass spectroscopy. We thus propose to construct the neutron detector arrays NEBULA (**Ne**utron-detection system for **B**reakup of **U**nstable-nuclei with **L**arge **A**cceptance), associated with the SAMURAI magnetic spectrometer in RIBF. NEBULA should determine **momentum vectors of neutron(s)** emitted in the breakup reaction of unstable nuclei.

Requirements of NEBULA we set are as follows.

a. It should have **a large acceptance** sufficient for the detection of neutrons emitted in the breakup reactions of neutron-rich unstable nuclei up to a relative energy of **10 MeV** (corresponding to the order of one-neutron separation energy). This large coverage of energy is necessary for the study of giant resonances of neutron-rich nuclei by Coulomb dissociation and nuclear dissociation.
b. It should have **a good energy resolution** for obtaining the excitation energy spectrum in the invariant mass spectroscopy.
c. It should detect **multi-neutron coincidence events**. Our goal is that NEBULA is able to unambiguously detect **4 neutrons** in coincidence. At the RIBF facility, 4n-core system ^{8}He, ^{19}B as well as unbound 4n ,^{5}He are to be investigated in detail. Those systems are expected to break up into 4n + (core fragment) with large probabilities, and 4-neutron measurement is thus necessary.

[2-3-2] Typical Setup of NEBULA

Figure 2-3-1 shows typical setups for the reaction $^{A}Z \rightarrow ^{(A-1)}Z+n$ (1-neutron breakup, Fig. 2-3-1 (a)) and the reaction $^{A}Z \rightarrow ^{(A-4)}Z+4n$ (4-neutron breakup, Fig. 2-3-1 (b)). Also shown in Fig. 2-3-2 is a 3-dimensional schematic drawing of NEBULA corresponding to Fig. 2-3-1(b).

We propose that NEBULA is composed of 240 modules of plastic scintillators (e.g. BC408). Each module has a dimension of 12cm(D)x 12cm(H) x 180cm(V), coupled to photomultiplier tubes (PMT) at both vertical ends. The segmentation determines the horizontal(x), and the distance (z) coordinates of the hit position, while the time difference observed between two PMT's determines the vertical coordinate (y). The coordinates together with the time of flight (TOF), determined by the mean time of two PMT's, will

provide the momentum vector of each neutron. Besides the main neutron detectors, NEBULA is also equipped with one or more layers of thin scintillators for charged particle veto. As later described, for multi-neutron detection, we impose a kinematical condition to unambiguously detect multiple neutrons, which require a certain separation of detector positions. For the case of 4 neutrons we need 4 sets of 'stacks' which are separated by about 1m, respectively. For n-neutrons, in principle, n sets of stacks are necessary. For a single neutron detection, such separation is not necessary as shown in Fig.2-3-1(a). As a typical setup for multi-neutron detection, one stack is composed of two layers of plastic scintillators associated with one layer of thin plastic scintillator for veto. The flexibility of setup configuration is thus important.

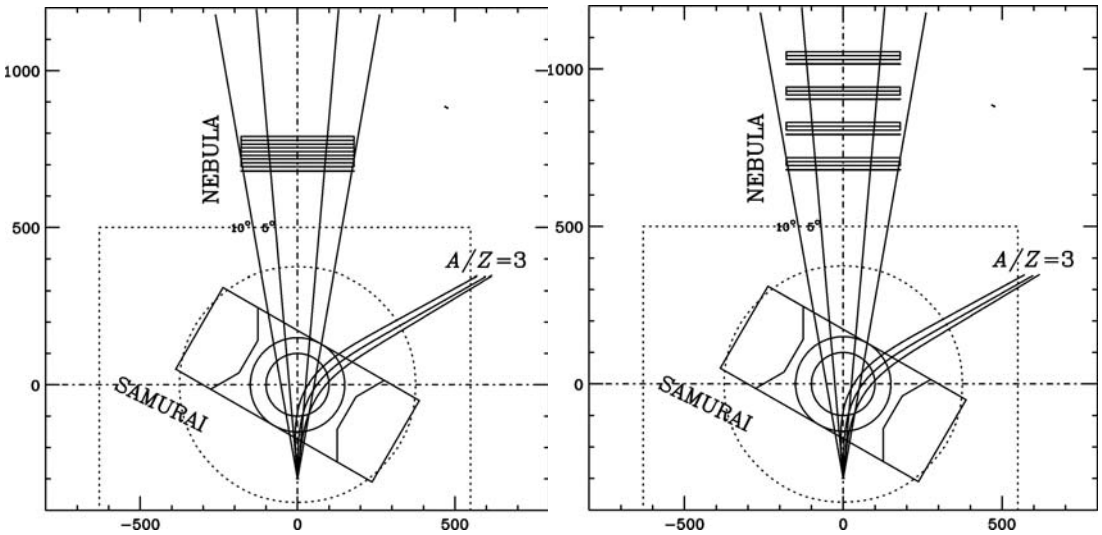

Fig. 2-3-1 (a)Left: Typical setup of NEBULA for one-neutron breakup reaction together with SAMURAI magnet (30deg rotated). (b)Right: Typical setup of NEBULA for four-neutron breakup reaction.

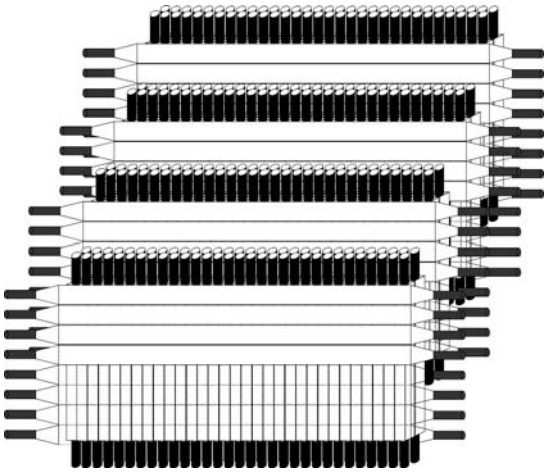
Fig. 2-3-2 A schematic drawing of NEBULA setup for 4 neutron detection. The setup is composed of 4 stacks; each stack is composed of two layers of neutron detectors associated with one layer of thin veto scintillators. Half of vetos are drawn as skeleton for showing off the neutron detectors behind.

Next, We describe the method of unambiguous detection of multi-neutrons, and study how the separation between each stack should be.

[2-3-3] Acceptance consideration

[2-3-3-1] Importance of neutron acceptance

In the breakup reaction of projectile for invariant mass spectroscopy, the acceptance for neutrons is much more critical than the charged fragment emitted simultaneously. Take an example of a one-neutron breakup reaction $^{A}Z \rightarrow ^{(A-1)}Z+n$, where the n-charged fragment relative energy E_{rel} is written approximately as,

$$E_{\mathrm{rel}} \approx \frac{\mu}{2}\left[\left(\frac{v_n - v_C}{\gamma}\right)^2 + \left(\bar{v}\theta_{nc}\right)^2\right], \qquad (1)$$

where v_n, v_c represent respectively outgoing velocities of neutron and charged particle fragment, $\bar{v}$ the mean velocity of neutron and charged particle, and θ_{nc} the opening angle between two outgoing velocity vectors. The kinematics of this breakup reaction (for non-relativistic case for simplicity) is shown in Fig.2-3-3. As clearly seen from the diagram, the recoil velocity for neutron is larger by 1/(A-1) than that of the charged fragment, in the center of mass of two outgoing particles. Consequently, the angle for the neutron is almost identical to the opening angle as in $\theta_n \approx (A-1)\theta_c \approx \theta_{nc}$. This implies that the acceptance is dictated by the neutron.

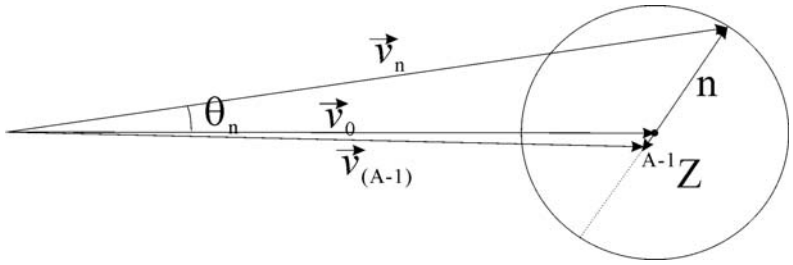

Fig.2-3-3 Velocity diagram for the breakup reaction $^{A}Z \rightarrow ^{(A-1)}Z+n$.

It is useful to extract the approximate relation between the neutron angle θ_n and E_{rel}. The event with the maximum opening angle occurs when E_{rel} is solely determined by the opening angle $\theta_{nc}(\cong \theta_n)$, *i.e.*, $v_n = v_c$ in Eq. (1) , where

$$E_{\mathrm{rel}} \approx \frac{\mu}{2}\left(\bar{v}\theta_{nc}\right)^2 \approx E_n{\theta_n}^2 . \qquad (2)$$

This shows that at a certain E_{rel} the maximum angle of neutron can be approximately expressed as

$$\theta_n{}^{\max}(E_{\mathrm{rel}}) \approx \sqrt{\frac{E_{\mathrm{rel}}}{E_n}} \quad . \qquad (3)$$

For instance, at $E_{\mathrm{n}} = 250\ \mathrm{MeV}$, which is a typical neutron energy in the RIBF project, $\theta_n{}^{\max}(E_{\mathrm{rel}} = 1.9\mathrm{MeV}) = 5\,\mathrm{deg.}$, $\theta_n{}^{\max}(E_{\mathrm{rel}} = 7.7\mathrm{MeV}) = 10\,\mathrm{deg.}$ and , $\theta_n{}^{\max}(E_{\mathrm{rel}} = 17.8\mathrm{MeV}) = 15\,\mathrm{deg.}$

Thus, a full coverage of angles up to 5, 10, 15 degrees is necessary to fully accept the events with

E_{rel} =1.9, 7.7, and 17.8 MeV, respectively. These values can be benchmarks for considering the acceptance of the neutron detectors.

[2-3-3-2] Simulation for the acceptance curve for one-neutron breakup

We have performed simulations for estimating the acceptance by using the code ACC[1]. In this code, the nucleus ^{A}Z is broken up into $^{(A-1)}$Z + n which are emitted isotropically in the center of mass of A system with a certain relative energy. The center of mass system is scattered off by θ_{sc} from the beam axis in the projectile+target center of mass frame. This code also takes into account a finite spread of the beam. Here, we set the reaction to be a one-neutron breakup of ^{31}Ne at 250 MeV/nucleon on a Pb target.

As a conclusion of the simulations, we have found that the neutron angular-coverages of $-5^{\circ} \le \theta_{\mathrm{V}} \le 5^{\circ}, -10^{\circ} \le \theta_{\mathrm{H}} \le 10^{\circ}$ are at least necessary in order to meet the condition that the acceptance for E_{rel} up to 10 MeV is sufficient (about 50%), and the acceptance curve as a function of E_{rel} is rather smooth. This requires the SAMURAI magnet to have a sufficient gap size to permit neutron transmission. The present specification of the gap size (80 cm) meets this requirement. In what follows, the details of the simulation are described. In particular, we have investigated how the acceptance shape (rectangular or square) in the neutron detection coverage affects the acceptance curve for E_{rel}. We also compare our result with the setup planned at GSI.

[2-3-3-2-1] Simulation result with a fixed vertical angular coverage

The left panel of Fig.2-3-4 shows the result of simulations for the E_{rel} acceptance curves with a vertical angular coverage being fixed to $-5^{\circ} \le \theta_{\mathrm{V}} \le 5^{\circ}$. We have performed simulations for four cases with different horizontal angular coverages, *i.e.* Cond.1: $-5^{\circ} \le \theta_{\mathrm{H}} \le 5^{\circ}$, Cond.2: $-10^{\circ} \le \theta_{\mathrm{H}} \le 10^{\circ}$, Cond.3: $-15^{\circ} \le \theta_{\mathrm{H}} \le 15^{\circ}$, and Cond. 4: $-20^{\circ} \le \theta_{\mathrm{H}} \le 20^{\circ}$. The incident energy is fixed to 250 MeV/nucleon, and the scattering angle is generaged as a uniform distribution between 0-1 degrees.

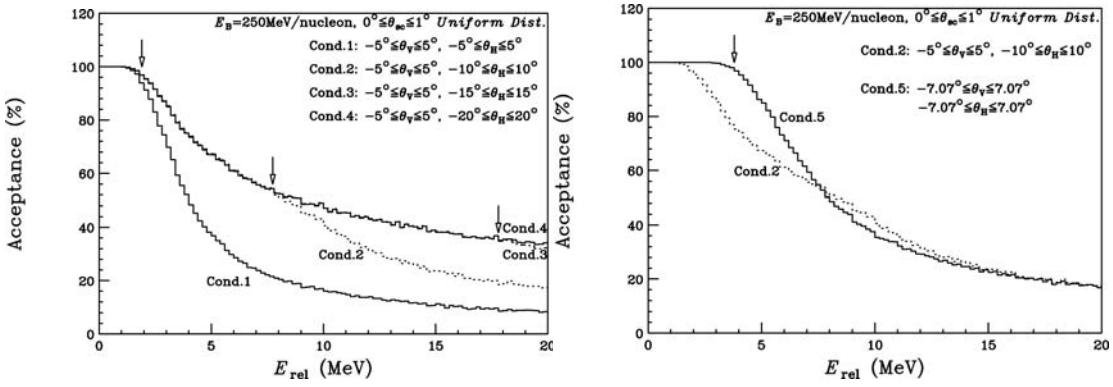

Fig. 2-3-4 LEFT: Comparison of acceptance curves for E_{rel} (0-20MeV) with the vertical angular coverage fixed to $-5^{\circ} \le \theta_{\mathrm{V}} \le 5^{\circ}$, estimated for one-neutron breakup of ^{31}Ne→$^{(A-1)}$Ne+n at 250 MeV/nucleon. Arrows show separation points for 4 conditions of angular coverage shown in the text. RIGHT:

Comparison of acceptance curves for E_{rel} with the solid angle fixed to 62msr. The effect of shape difference of angular coverage is observed.

The result has interesting features, showing where curves for four conditions are going apart at certain E_{rel} values. Namely, at 1.9 MeV (shown by an arrow), the curve for Cond.1 is separated from others and falling down sharply, at 7.7 MeV (shown by an arrow) the curve for Cond.2 is separated, at 17.8 MeV (also shown by an arrow) the curve for Cond.4 is finally separated from that for Cond.3. This is easily understood by the fact that these energy values correspond to those whose maximum angles $\theta_n^{\max}(E_{\mathrm{rel}})$ are 5, 10, and 15 degrees, respectively. Since the relative energy of 8 MeV corresponds to a typical location where the two neutron breakup channel begins to open, the chances of neutron emission over this relative energy is becoming smaller. Hence, the Cond.2 is considered to have the most appropriate angular coverage when fixing the vertical angular coverage.

[2-3-3-2-2] Simulation result with a fixed solid angle

The right panel of Fig.2-3-4 shows the result of simulations for the E_{rel} acceptance curves with the solid angle being fixed to 62mrad. The case of Cond.2. ($-5^{\circ} \le \theta_{\mathrm{V}} \le 5^{\circ}, -10^{\circ} \le \theta_{\mathrm{H}} \le 10^{\circ}$) has this solid angle, and the same solid angle can be covered by the square shape of $-7.07^{\circ} \le \theta_{\mathrm{V}} \le 7.07^{\circ}$ and $-7.07^{\circ} \le \theta_{\mathrm{H}} \le 7.07^{\circ}$(Cond.5). This simulation is to investigate how the shape of the angular coverage affects the E_{rel} acceptance curve. A square coverage is, for instance, taken in the GSI future project (80mrad x 80mrad (4.6deg x 4.6deg)). In the figure, the arrow corresponds to the energy whose $\theta_n^{\max}(E_{\mathrm{rel}})$= 7.07 degrees. It is thus natural that up to this energy the acceptance is almost 100%. The curve for Cond.5 is then falling more rapidly than the case of Cond.2 over this energy since Cond.2 has a larger horizontal angular coverage. Thus there is a certain range around E_{rel} =10 MeV, where Cond.2 wins over Cond.5. Finally, these two curves converging at larger E_{rel} as is expected. In conclusion, the effect of shapes in terms of shapes is not so strong except in these minor points.

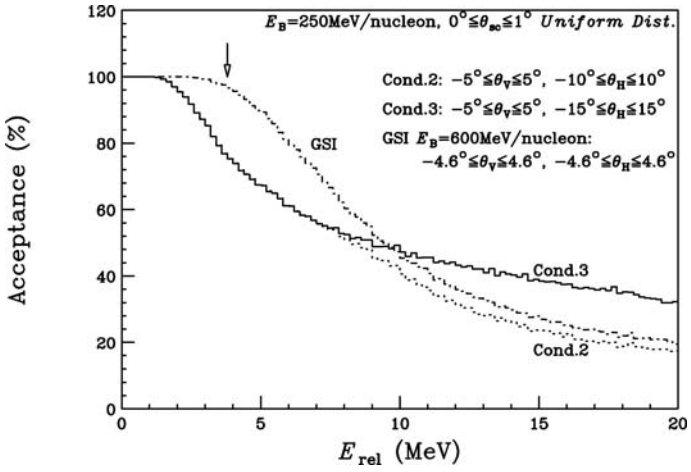

Fig. 2-3-5 Comparison of acceptance curves for Cond.2, Cond.3 at 250 MeV/nucleon, and GSI case at 600 MeV/nucleon.

Also shown in Fig.2-3-5 is a comparison with the GSI case, where we assume the mass ^{31}Ne with 600 MeV/nucleon breaks up into ^{30}Ne and neutron. We have found that the GSI case is quite similar to the case for Cond.5 at 250 MeV/nucleon. Up to the arrow point, the GSI case has 100% acceptance, and overall wins over Cond.2 at 250 MeV/nucleon. However the difference between the GSI case and Cond. 2 is only about 20%. When considering our beam intensity is much larger than GSI, Cond. 2 is acceptable in terms of the competition with GSI. We should note that the Cond.3 is potentially possible at the current SAMURAI magnet specification since it has a larger gap space in the horizontal direction.

[2-3-3-3] Simulation for the acceptance curve for two-neutron breakup

It is important to understand how the acceptance curve is changed when the number of emitted neutrons in each event is increased. Fig.2-3-6 shows the results of the simulation for evaluating the acceptance for two neutrons in the 2n breakup reaction (we assume the breakup reaction of ^{32}Ne→^{30}Ne+n+n at 250MeV/nucleon). The neutron setup used here is L=10m, ΔL=0.76m with area of 3.6m(H) x 1.8m(V) in the setup shown in Fig. 2-3-8. With this setup the rear face of W1 covers $-5^{\circ} \le \theta_{\mathrm{V}} \le 5^{\circ}$, and $-10^{\circ} \le \theta_{\mathrm{H}} \le 10^{\circ}$(Cond.2), and the rear face of W3 covers $-4.6^{\circ} \le \theta_{\mathrm{V}} \le 4.6^{\circ}$, and $-9.2^{\circ} \le \theta_{\mathrm{H}} \le 9.2^{\circ}$. Also shown in the figure is that the 1n acceptance in the 1n breakup reaction (Cond.2) and that in the 2n breakup reaction. The figure shows that the 2n acceptance in the 2n breakup channel is almost identical to the 1n acceptance in the 1n breakup channel. It should also be noted that the 1n acceptance in the 2n breakup channel is much larger than that in the 1n breakup channel. The reason is that the relative energy of the core-n is always smaller than the core-n-n relative energy in the 2n breakup channel. In fact, on average, the core-n relative energy is about half the core-n-n relative energy when 2n+core is emitted in a democratic phase space (i.e. emitted uniformly in the dalitz plot). This indicates that the multiple neutron detection does not hinder the acceptance.

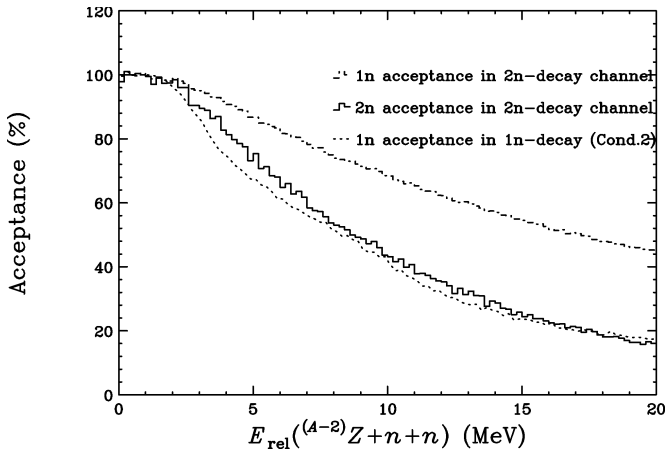

Fig. 2-3-6 Acceptance curve for the 2n detections in the 2n breakup reaction is compred with the 1n acceptance for the 2n breakup reaction, and 1n acceptance for the 1n breakup channel. It shows that the acceptance for 2n is not so different from that for 1n in the 1n breakup. This is due to the fact that the

core-n relative energy is on average about half the three-body relative energy so that the 1n acceptance in the 2n breakup channel as a function of the three-body relative energy is enhanced as shown.

[2-3-4] Simulation for light output

In scintillation detectors, as is to be used in NEBULA, characteristics of the light output determine the timing resolution, which is essential in neutron detections. Not only for the TOF resolution, but also the position resolution in the longer direction (vertical direction in this case.) requires a good timing resolution. Timing resolution is also critical for the multi-neutron detection as later described. Here, by using the simulation code GUIDEM. we examine how the shape of the scintillator affects the number of photons, and thus timing resolution.

[2-3-4-1] Simulation of light output from a simple plastic scintillator

We simulate how the dimension of a simple plastic scintillator affects the number of photons and timing resolution. As an example, we take here a scintillator with a bar shape as shown in Fig. 2-3-7. The light source (10000 events) is set at the center of the cross section at a position *Y*. Photons are observed either on the top or bottom surface. In Table 1, the number of photons N_{bot} ,N_{top} , timing T_{bot}, T_{top},, and their widths in sigma, and the timing resolution ΔT are shown respectively for the bottom and top surfaces by changing the values of *L* and *W* (see Fig.2-3-7). The number of photons, 10000, corresponds to about 1 MeVee (assuming 100eV/photon) light output at the source. The timing resolution is estimated as in

$$\Delta T = \sigma / \sqrt{N \varepsilon_A \varepsilon_Q} \text{ , (4)}$$

where ε_A represents the efficiency of the acceptance of the photons on the surface penetrating into a PMT, while ε_Q the quantum efficiency of PMT. Here we assume $\varepsilon_A = S / W^2$, where S stands for the area of the cathode surface of PMT (2”=5.08cm in diameter in the current simulation), and ε_Q=10%. As an attenuation length of the scintillator we use λ=210 cm (catalogue value for BC408). The surfaces, other than the bottom and top ones, are covered by METAL (default option for GUIDEM).

The 1st and 2nd columns compare the effects with different *L*. This is basically determined by the value of λ, and the number of photons are thus different by about ln *2* (=0.69) as is expected. It is reported that the timing resolution is proportional to $\sqrt{L}$ [3]. We have found that the simulation follows roughly this rule.

The 1st and 3rd columns compare the effects with different W. We have found the number of photons, timing, and its width are almost identical for these two cases. This is due to the fact that the number of photons conveyed up to the top and bottom surfaces are dictated by the solid angle determined by the refractive index (n=1.5 is adopted here.). The difference of the timing resolution is due to the difference of ε_A. Since the cross section for the case of 3rd column matches the size of PMT better, the ε_A value is larger. We have to further investigate how this can be improved by coupling the light guide for wider W value.

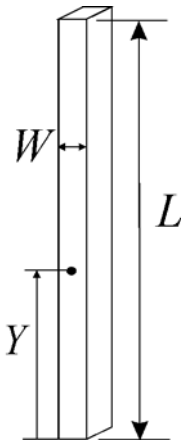

Fig. 2-3-7 A piece of scintillator (WxWxL) used for the light output simulation. The photon source with 10000 events is set at *Y*. Photons are observed on the bottom or top surface.

L (cm)	W (cm)	Y (cm)	N_{bot}	N_{top}	T_{bot} (ns)	$\sigma(T_{bot})$ (ns)	resol. (ns)	T_{top} (ns)	$\sigma(T_{top})$ (ns)	resol. (ns)
200	12	100	652	689	5.72	0.47	0.16	5.68	0.52	0.16
100	12	50	874	918	2.78	0.38	0.11	2.79	0.35	0.10
200	6	100	636	607	5.64	0.55	0.09	5.67	0.54	0.09

Table 1. Results of simulation by GUIDEM for a scintillator with a bar shape as in Fig. 2-3-7. The point light source (10000 events) is set at the center of the cross section at *Y*. Photons are observed either on the top or bottom surface.

[2-3-5] Detection of multi-neutrons

For detecting more than two-neutrons unambiguously, it is necessary to overcome the cross-talk events. Here by using the DEMONS code[4], which was developed for neutron detectors composed of segmented modules, we investigate what method and what configuration of setup is effective to measure two-neutron (or more neutron) events.

For simplicity, we take an example of the two-neutron breakup reaction, $^{A}Z \rightarrow ^{(A-2)}Z+n+n$. We are considering a setup shown in Fig. 2-3-8, where we use a two separate stacks, each having a two layers of neutron detectors and one thin veto layer (V1(veto),W1,W2), and (V2,W3,W4). The separation is essential for distinguishing true events from false cross talk events. Fig.2-3-8 shows two types of cross talks. The upper panel shows a cross talk with a different-wall type. As shown in the figure, when one neutron is emitted and hit a detector in W1, then this can be scattered out and hit another detector module at W3. This mimics an event where one neutron hits the detector module at W1 and another neutron hits the detector module at W3, namely a two-neutron event. Cross talk occurs also within the same stack as shown in the

bottom panel of Fig. 2-3-8 (same-wall type). As a first trial, we take a configuration with plastic scintillator modules, each has a dimension of 12cm(D) x 12cm(H) x 180(V) cm, with L=1012cm and ΔL=150cm. Timing resolution was set to be 350 ps in the code.

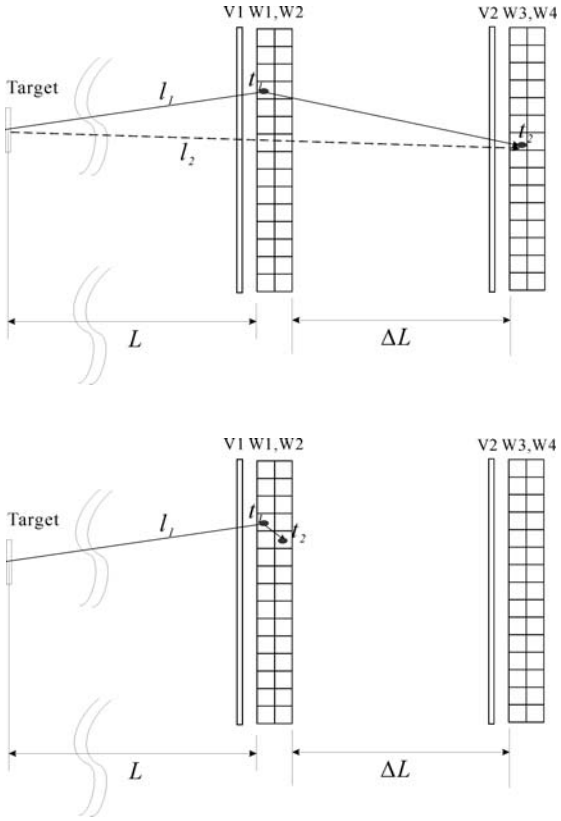

Fig.2-3-8 Examples of cross talks occurred for one neutron emission event. The upper panel is a different-wall type, and the lower-panel shows a same-wall type. See text for details.

[2-3-5-1] Exclusion of cross talks of same-wall type

As shown in Fig.2-3-8 (bottom), the cross talk within the same stack creates a multiple hits within a very narrow range. This means that if the two hits are observed with a certain short distance, we take this event to be caused by a single neutron. Shown in the Table 2 are number of events according to the multiplicity (M) for **the one-neutron breakup reaction** at 70 MeV and 250 MeV, simulated by DEMON for the setup shown in Fig. 2-3-8. "One neutron breakup" events are used in order to evaluate how the cross talks occur since all the higher multiplicity except M=1 is taken as a cross talk. Here, the multiplicity is defined as a number of detector modules with the light output over the threshold (V_{th}) of 6 MeVee. The 1st and 2nd columns show bare numbers, while the 3rd and 4th columns show the numbers after consideration of the "clustering procedure" in the same stack. Here, the clustering procedure is made such that when the two hit positions are close enough according to a certain condition, then these are summed up as a single neutron event. The condition taken here is that detector ID numberp is adjacent (0,or +1, or -1), and their position difference in y is within 20 cm.

Multiplicity	M1	M2	M3	M4
En=70 MeV w/o clustering	41146	4876	75	0
En=250 MeV w/o clustering	20116	9072	7155	2546
En=70 MeV w clustering	44441	1650	0	0
En=250 MeV w clustering	29600	9397	347	4
En=250 MeV w clustering, w 2nd veto	33621	2567	82	0

Table 2. Number of events for multiplicity=1,2,3,4 for single-neutron events (100000 events) at E_n=70 MeV, and 250 MeV. The upper two columns are bare numbers, while the lower two columns show the numbers with clustering being included. The last column shows the values with validation of the 2nd veto detectors.

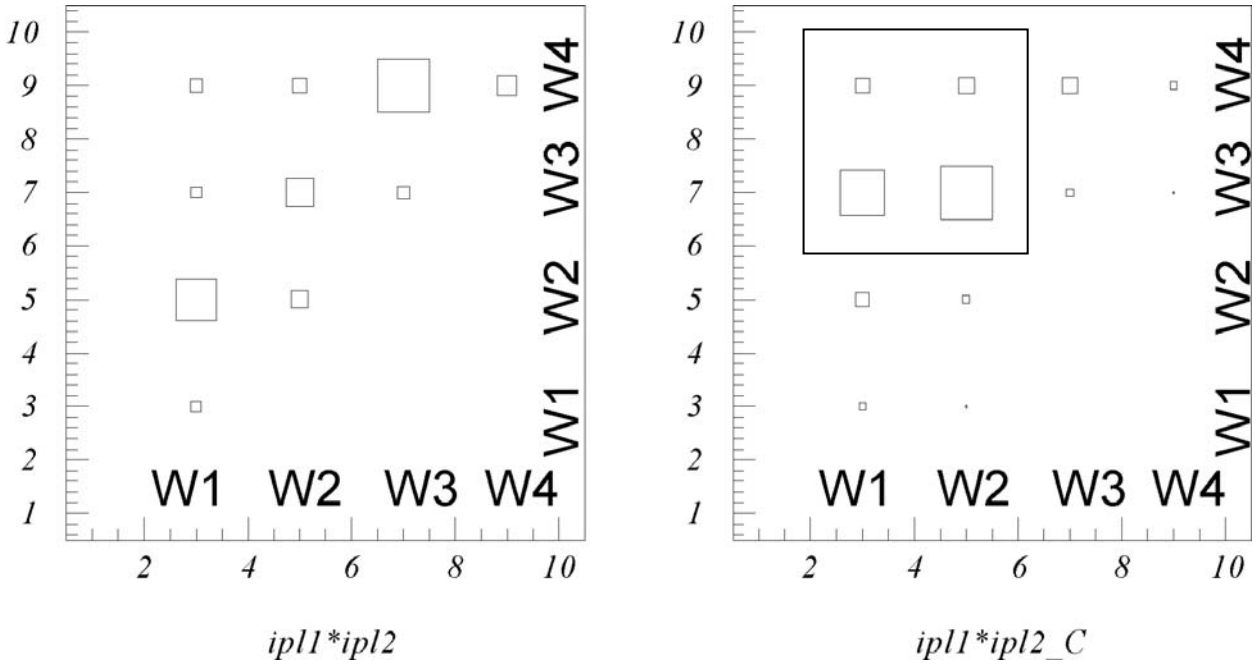

Fig.2-3-9 The hit pattern for M=2 events without clustering procedure (left), and with clustering procedure (right). With the clustering procedure, the cross talk in the same wall event (W1xW2,W3xW4) will be significantly reduced. Meanwhile, the different wall event (e.g. W1xW3,W2xW3, surrounded by a square) has increased (*from M=3 event originally*).

In the case of a neutron at 70 MeV, the clustering procedure does not have much effect for increasing the number of M=1. On the other hand, for 250 MeV, the clustering procedure is essential. Otherwise, even a single neutron as in the present case can be detected as 3-neutron or 4 neutron events. Hit patterns for M=2 are plotted in Fig. 2-3-9 to illustrate how the clustering procedure is effective. M=2 events remaining here (in particular shown in the box boundary) will be further removed by validating the 2nd veto detector and the different-wall cross talk analysis (sec. 2-3-5-2) as described later.

The disadvantage of removing cross talks of the same-wall type is that a true two-neutron event with very small relative energy can be observed as a “one-neutron event” after the clustering procedure. This essentially reduces the efficiency at low relative energies. For this reason, we also need a separate stack setting (different-wall event analysis) as discussed in the next section

[2-3-5-2] Exclusion of cross talks of different-wall type

In the case of cross talks of different-wall type, we can make use of kinematical conditions. In Fig. 2-3-8 (top), we showed a typical cross talk occurred as a different-wall type. In this case, the scattered neutron has less kinetic energy than the initial kinetic energy. Consequently, the velocity β_1 determined by l_1, t_1, and apparent velocity β_2 determined by l_2, t_2 has a relation of $\beta_1 > \beta_2$. If we impose a condition $\beta_1 \leq \beta_2$, then the cross talk event will be completely removed. The advantage of this method is that we can measure up to the zero relative energy between two (or more) neutrons. This, however, also depends on the timing resolution (and flight path resolution) determining these velocities. In the next section we estimate the efficiency of this removal method by DEMONS.

[2-3-5-2-1] Importance of veto for the second stack

As shown in Fig. 2-3-9(right), there remain a significant number of different-wall cross talk events as shown by the box surrounding region. We have found that most of these events are in fact coming from the recoil proton from W1 or W2 going to W3. For avoiding these charged particle generated in the first stack, the second veto layer (V2) is installed as in Fig.2-3-8 (N.B. the simulation above did not validate V2.) The V2 is used such that when V2 has a signal, the signals in the second stack (W3, W4) are neglected. For example, when W1, V2, W3, W4 have fired, this is interpreted as only W1 has a signal and thus the multiplicity is one. By using this procedure, the multiplicity distribution is much improved, as shown in the last column of Table 2. In fact, the number of M1 events has increased, while the number of M2 events has reduced significantly. With this procedure, there remain 683 cross talk events due to the different wall.

[2-3-5-2-2] Removal of cross talk by kinematical condition

Fig. 2-3-10 (left) shows the $\beta_1 - \beta_2$ spectrum for the remaining 683 different-wall events. It clearly shows that most of the events have positive values, indicating the energy loss in the first scattering. Only a small number of events (41 events, or only 0.11% of the total number of M1 events) remains as indistinguishable cross talk events.

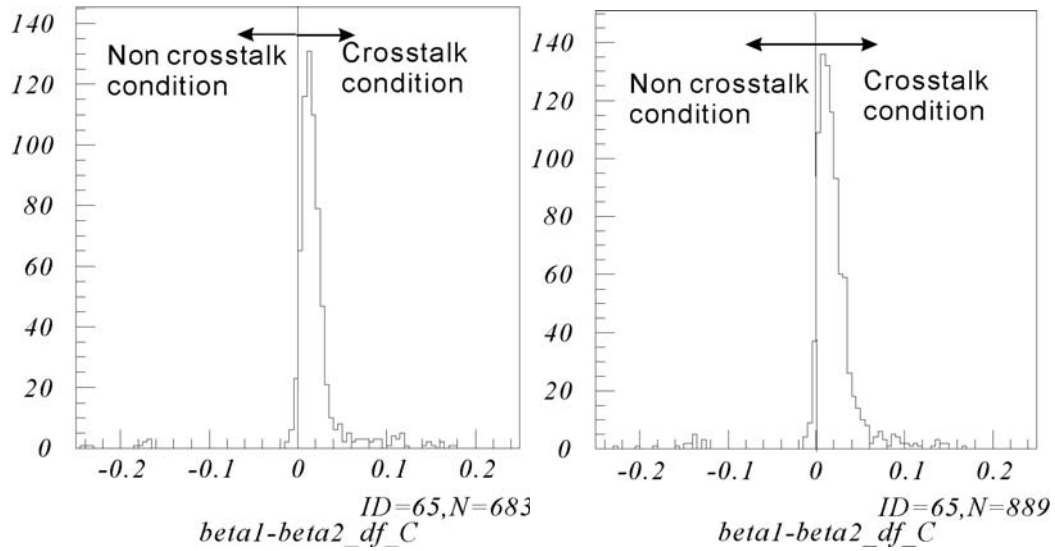

Fig.2-3-10 $\beta_1 - \beta_2$ spectrum for the setup with ΔL=150cm (left) and ΔL=50 cm (right).

[2-3-5-2-3] Estimation of cross-talk removal efficiency

As shown in the previous section, the case with ΔL =150 cm with W=12 cm, δT=0.35ns gives finally the fraction of indistinguishable events as 0.11%. In reality we have to compromise this value with the restriction of the setup, where ΔL is to be as short as possible. When ΔL is larger then the acceptance is accordingly reduced. Also, we should note the event where a neutron is scattered with no signal (or signal less than threshold) and then makes signal at the downstream wall. In this case, the position information is less accurate when ΔL is larger. We should certainly simulate this effect in the near future.

Here, we examine how the values of ΔL, W, δT affect the indistinguishability of cross talk events of the different wall type. For this estimation, we introduce the efficiency of indistinguishability (ε_{non}). This is defined as follows. Firstly we label $\varepsilon_1, \varepsilon_2$ as M=1 neutron efficiencies for W1,2, and W3,4, respectively. ε_{non} is estimated as how many events in one-neutron removal events (n+core events) are mistaken as two-neutron removal events (n+n+core events). We define the two-neutron removal cross section as σ^{-2n} (2n is emitted in the reaction and both neutrons penetrates the neutron detectors), and from one-neutron cross section as σ^{-1n} (1n is emitted in the reaction and this neutron penetrates the detectors). The number of detected events for one-neutron removal event is written as $N_1 = C\sigma^{-1n}(\varepsilon_1 + \varepsilon_2)$, while that for two-neutron removal event is $N_2 = C\sigma^{-2n}({\varepsilon_1}^2 + {\varepsilon_2}^2 + 2\varepsilon_1\varepsilon_2)$, while C is a common factor determined by the number of atoms/cm^2 and in a target and beam intensity. In the case of different-wall 2n-removal events after removal of cross-talk events, $N_2{}^d = C\sigma^{-2n}\varepsilon_1\varepsilon_2$, a cross talk event from a one-neutron removal event is described as $N_1^c = C\sigma^{-1n}(\varepsilon_1 + \varepsilon_2)\varepsilon_{sv} = N_1\varepsilon_{sv}$, where ε_{sv} is a ratio of indistinguishable cross talk events to the total number of M=1 events (in the case of ΔL =150 cm with W=12 cm, δT=0.35ns in the previous section, this was 0.11%). Consequently the ratio of cross talks mixed in the two-neutron removal events is described as,

$$\varepsilon_{non} = \frac{N_{1c}}{N_{2d}} = \frac{\sigma^{-1n}}{\sigma^{-2n}} \frac{\varepsilon_1 + \varepsilon_2}{\varepsilon_1 \varepsilon_2} \varepsilon_{sv} \quad (5)$$

Here for simplicity we assume the ratio $\sigma^{-1n} / \sigma^{-2n}$ to be unity, and estimate ε_{non}. The result for several cases with ΔL, and W=12cm, 6cm are shown in Table 3. We fix the timing resolution of δT=0.35ns. We found that the change of the resolution to 0.25 ns does not affect very much. (ε_{non}=2.1%-->1.9% for ΔL =100cm and W=12cm). On the other hand, the change of W=12cm to 6 cm significantly improves the situation. In the case of W=6cm, ε_{non} value for ΔL=50 cm is almost similar to that for ΔL=100 cm with W=12cm. In this sense, if we need a very good efficiency up to very low relative energies for multi-neutron detections, W=6cm is preferable than W=12cm setup.

ΔL (cm)	W (cm)	N(M=1)	N(M=2)	ε_1 (%)	e_2 (%)	N_{non}	ε_{sv} (%)	ε_{non} (%)
50	12	35239	3682	18.3	16.1	126	0.36	4.2
100	12	35445	2994	19.1	16.3	66	0.19	2.1
150	12	36321	2567	20.3	16.0	41	0.11	1.3
50	6	20263	780	10.5	9.8	30	0.15	2.9
100	6	21136	690	10.6	9.8	15	0.07	1.4
150	6	20440	589	10.8	9.6	10	0.05	1.0

Table 3. The efficiency of cross talk exclusion procedure in different wall events.

[2-3-6] Calibration Method

Here we propose the setup where each neutron detector module is in the vertical direction (longest part is in the vertical direction). In this case, the cosmic ray calibration becomes very difficult since the flux to the horizontal direction is necessary in this case, and this is much rarer than the vertical events.

Instead, we propose to make use of a proton beam. In the RIBF project, we expect an H_2^+ molecular beam with 440 MeV/nucleon. This beam has a stopping range of 96.7 g/cm^2 (93.7 cm), which almost covers the current setup (96cm). The SAMURAI magnet with the different polarity, and different current setting can be used to sway the proton beam. Also the RF deflector can be used to swing the beam up and downwards to a certain degree.

For calibration purposes, in any cases, it is better that the detector can be movable with ease. We propose that each stack (1V+2walls) can be made in one structure, and can be movable.

[2-3-7] Budget Consideration

We evaluate the values for W=12cm case. (Although 6cm case is more ideal, the budget is too big (about double) in that case).

W=12cm	**Scintillators**	**~100 M JPY**
	PMT	**~ 60 M JPY**
	Electronics	**~50 M JPY**
		~ 210 M JPY

[2-3-8] Man power

T. Nakamura(Tokyo Tech.), Y. Satou(Tokyo Tech.), K. Yoneda (RIKEN), T. Motobayashi (RIKEN), a post doc (RIKEN or Tokyo Tech), and 2-3 Ph.D course students (Tokyo Tech.).

[2-3-8] Schedule

FY2006 R&D

FY2007 construction

FY2008 electronics & test, calibration

References

[1] ACC: Acceptance simulation code, unpublished, T. Nakamura (2004).

[2] GUIDEM: simulation code for light output by K.McFarlane (NSU and JLAB), which is a modified version of GUIDEIT by D.A. Simon. GUIDEIT itself is also a modified version of GUIDE 7 in the CERN code.

[3] R.C. Byrd, et al., NIM A 313, 437 (1992).

[4] DEMONS: simulation code for neutrons developed in LANL

[2-4] Detector system for (γ,p)-type measurement in the proton-rich region

[2-4-1] Measurement of proton decay channel

We propose here studies of the proton unbound states in the proton rich region to which the RIBF project can provide good access. In order to examine nuclear structure of nuclei close to, or beyond, the proton drip line, measurements of the location of the unbound states are critical. For astrophysical interest, studies of proton unbound states are also important, since the energy and width of such states influence radiative capture cross sections under astrophysical conditions, and hence play an important role in exploring nucleosynthesis processes.

Such unbound states are identified with the invariant mass method, through the measurement of the kinetic energies and scattering angles of breakup products. For two body breakup reactions, the invariant mass is defined as,

$$M_{inv} = M_1 + M_2 + E_{rel} = \sqrt{(E_1 + E_2)^2 - (\vec{P}_1 + \vec{P}_2)^2} = \sqrt{(E_1 + E_2)^2 - P_1^2 - P_2^2 - 2P_1P_2\cos\theta_{open}} ,$$

where θ_{open} is the opening angle between the two breakup products. The energy of relative motion is extracted to be $E_{rel} = M_{inv} - M_1 - M_2$. Coulomb dissociation using heavy-mass targets has been used commonly, but we also plan to investigate proton breakup reactions induced by light probes such as liquid hydrogen, deuteron, and helium targets. Knockout reactions feeding to proton unbound states will also be studied.

[2-4-2] Required angular and momentum acceptances

The maximum opening angles between heavy ions of A/Z∼2 and proton for two body breakup reactions is calculated to be,

$$\theta_{open} < \cos^{-1}\left(1 - E_{rel}/(\mu c^2 \gamma^2 \beta^2)\right),$$

where μ is the reduced mass. In the case of E_{rel} = 1 MeV and E_{in} = 250 A MeV and $\mu \sim m_p$, the maximum opening angle is 3.4 degrees (59 mrad). The angular acceptance is hence required to be at least ±60 mrad. The scattering angles of the heavy ions are smaller; in Coulomb dissociation and proton inelastic scattering the scattering angles are typically a few degrees and less than 0.5 degrees, respectively.

The momentum acceptance is required to be p_{max}/p_{min}∼3, so that both of the proton and reaction fragment are measured in coincidence.

[2-4-3] Required angular and momentum resolutions

For two body breakup reactions, the relative energy resolution is calculated as,

$$\delta E_{rel} = \delta M_{inv} = \sqrt{\left(\frac{\partial M_{inv}}{\partial \theta_{open}}\right)^2 \delta\theta_{open}^{\ 2} + \left(\frac{\partial M_{inv}}{\partial P_1 / P_1}\right)^2 \left(\frac{\delta P_1}{P_1}\right)^2 + \left(\frac{\partial M_{inv}}{\partial P_2 / P_2}\right)^2 \left(\frac{\delta P_2}{P_2}\right)^2} .$$

The condition of E_{rel} = 1 MeV and E_{in} = 250 A MeV and $\mu \sim m_p$ leads to $\frac{\partial M_{inv}}{\partial \theta_{open}} < 34.1\,\mathrm{keV/mrad}$ and

$\frac{\partial M_{inv}}{\partial P / P} < 130\,\mathrm{keV/\%}$. For low-lying resonance studies, 0.1 MeV (1σ) resolution at E_{rel} = 1 MeV is necessary to separate the states, especially in the (p,p'), (d,d'), (α,α') and knockout reactions. In order to obtain 0.1 MeV resolution at E_{rel} = 1 MeV, the opening angle resolution of 2 mrad and momentum resolution of σ_P/P =0.5% are required. The momentum resolution required for the mass identification is severer; σ_P/P = 0.2% is required for 5σ separation at A=100 region. This momentum resolution is similar to the rigidity resolution of 1/700 mentioned in Sec. 1.2.

[2-4-4] Experimental setup

We propose two experimental setups. One is the high resolution mode, in which proton-rich reaction residues around A/Z~2 are bent in the SAMURAI magnet as much as possible, so that a good momentum resolution is achieved. The other setup is the exclusive measurement mode, where the resolution is relatively worse but the forward angles are open for neutron detection. In the following these two modes are described.

[2-4-4-1] High resolution mode

Using the large acceptance spectrometer, we are planning to perform various experiments of Coulomb dissociation and proton inelastic scattering, such as ^{22}Si→^{20}Mg+2p (nuclear structure interest), ^{40}Ti→ ^{38}Ca+2p, ^{31}Cl→^{30}S+p (astrophysical interest) and knockout reactions, such as , ^{100}Sn→^{99}Sn*→^{98}In+p, ^{97}Cd+2p. The required relative energy resolution is 0.1 MeV in 1σ at E_{rel} = 1 MeV to resolve excited states separated by 0.3 MeV. Let us consider the case of the measurement of unbound excited states in ^{40}Ti. The states higher than the proton separation energy (1.97MeV) are not known but are expected, from its mirror nuclei ^{40}Ar, to be at about 2.12MeV, 2.52MeV, 2.89MeV, etc. In this case, separation of the states about 0.3 MeV apart is actually needed. To achieve this relative energy resolution, 2 mrad resolution for the opening angle and 0.5% momentum resolution are necessary. To achieve mass identification, which is used to identify other reaction channels such as ^{100}Sn→^{99}Sn*→^{98}In+p and ^{100}Sn→^{100}Sn*→^{99}In+p, a severer momentum resolution of 0.2% in 1σ is required.

Figure 2-4-1 shows a schematic view of the experimental setup for the high resolution mode. The particle trajectories are drawn for a 3T magnetic field. As one can see, the beam axis is shifted off center so that the particles pass through a longer magnetic field. If the beam axis is set in the middle of the magnet, 0.2% momentum resolution in 1σis achievable for both protons and reaction residues according to Monde Carlo simulations, without silicon detectors placed between the target and magnet (described shortly). However, in this condition the angular acceptance in the vertical direction of protons is too small (±44mrad: 2.5 degrees) and the angular resolutions are degraded by a large fringing field. By placing the magnet 30 cm left of the projectile axis as shown Fig. 2-4-1, the angular acceptance is improved to be about ±60 mrad due to the weak focusing effect. The angular acceptances calculated by Monte Carlo simulation using GEANT-3 are shown in Fig. 2-4-2.

In order to achieve the opening angle resolution of 2 mrad, silicon microstrip detectors are placed between the target and magnet to measure scattering angles of protons and heavy ions right after the target.

One may consider a gas detector, such as a drift chamber as proposed above, for this purpose, but the operation of such a detector is impossible under the condition that the detector is hit by both heavy and light particles we need to detect; if the high voltage is adjusted for protons, the detector is not operable when heavy particles hit the detector and generate too much charge. An option using plastic fiber scintillators was also considered, but we cannot use them, in terms of the homogeneity, in front of the high resolution spectrometer.

Two sets of three silicon microstrip detectors (in the horizontal, vertical, and diagonal directions) with a thickness of 0.1 mm and an active area of 140 mmϕ are located at 60 and 85 cm downstream of the target. The angular straggling of protons and heavy ions in a 0.3-mm-thick silicon is about 1.7 mrad and 1 mrad, respectively. To obtain 2 mrad opening angle resolutions, we have to measure scattering angles with a resolution less than 1.4 mrad at least. When two sets of microstrip detector of 0.2 mm pitch are placed 150 mm apart, the scattering angle can be measured with a resolution of 1.4 mrad from the tracks of the charged particles. Similar detector systems were used in the experiments of Coulomb dissociation of ^{8}B and ^{6}Li using the KaoS spectrometer at GSI.

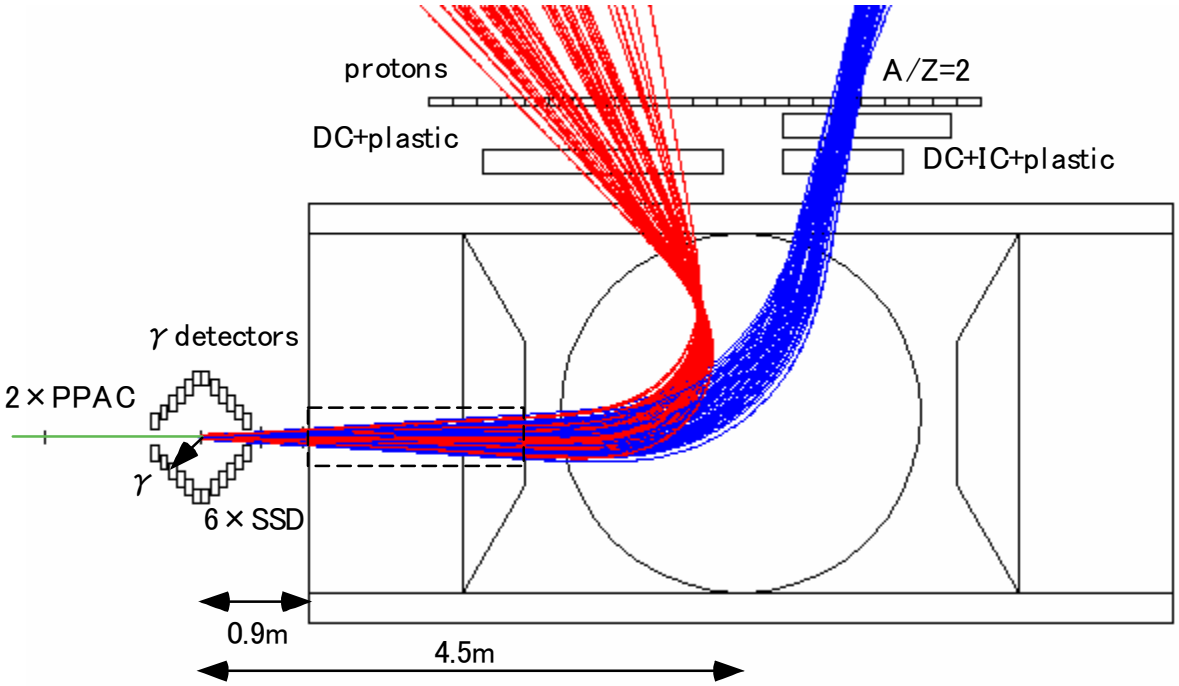

Fig. 2-4-1: Schematic view of the experimental setup for the high resolution mode. Detectors to be used and trajectories of proton and heavy ions of A/Z=2 at 250 A MeV scattered at θ= 0-4 degrees, ϕ = 0-2π are shown. The trajectories were calculated by Monte Carlo simulations using GEANT-3. A fraction of protons events are lost by hitting the yoke of the magnet.

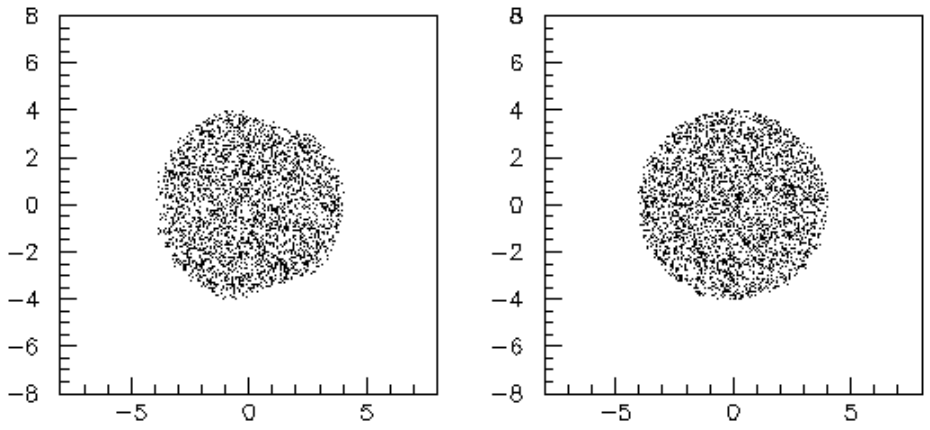

Proton A/Z = 2

Fig. 2-4-2: Angular acceptance, in degrees, of protons (left) and A/Z = 2 particles (right) in the vertical and horizontal directions calculated by Monte Carlo simulations using GEANT-3. Protons and A/Z = 2 particles were generated to fill a circular distribution of θ = 0-4 degrees and ϕ = 0-2π uniformly. For A/Z = 2 particles, a clear circle is seen suggesting no event loss, while some parts of events are lost for protons by hitting the magnet yoke.

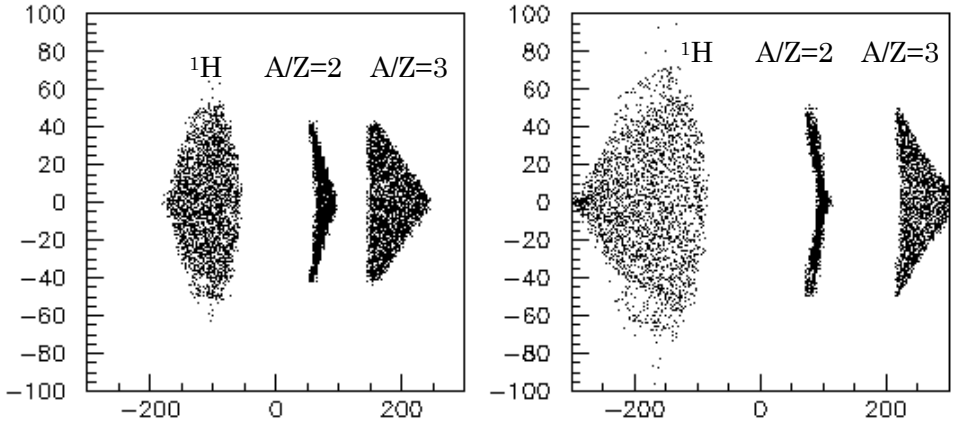

At drift chamber behind plastic scintillator wall

Fig. 2-4-3: Position on the focal plane detectors in cm calculated by Monte Carlo simulations using GEANT-3. Protons, A/Z = 2, and A/Z = 3 particles at 250 *A* MeV were generated at the target to fill uniformly in θ = 0-4 degrees and ϕ = 0-2π.

For the focal plane detectors for reaction fragments, we use a honeycomb cell drift chamber for position measurement, an ion chamber for energy loss measurement, and a plastic scintillator wall for TOF measurement. The detectors have an active area of about 1×0.8 m^2. The vertical width was determined from the gap of the magnet. Since the resolution of the plastic scintillators is not enough for charge identification of heavy ions, the ion chamber is used to identify the charge.

For focal plane detectors for protons, a huge honeycomb cell drift chamber ($2\times0.8m^2$) and

plastic scintillators are used. The large size of the detector covers defocused protons in both the horizontal and vertical directions as shown in Fig. 2-4-3. We are also considereing an option to install a smaller drift chamber (1×0.8 m^2) in the vacuum chamber in the magnet. To realize this option, R&Ds are needed concerning the gas pressure, foil thickness, and electric noises.

[2-4-4-2] Exclusive measurement mode

We are also considering another option of the setup shown in Fig. 2-4-4. In this setup, where the reaction products are injected to the magnet at 45 degrees with respect to the direction of the magnet yokes, the forward angles are available for neutron detection. This capability of the neutron detection in coincidence matches better to the basic concept of SAMURAI, namely, allowance of exclusive measurements for multi particles. This kind of setup is useful for experiments requiring multi particle coincidence measurement, for instance, (p, 2p+n) reactions to investigate proton-neutron short range correlations in nuclei. Furthermore, the setup is almost the same as (γ,n)-type reaction in Fig. 1-4a and b. It is a practical merit that we do not have to change things significantly from one experiment to the next.

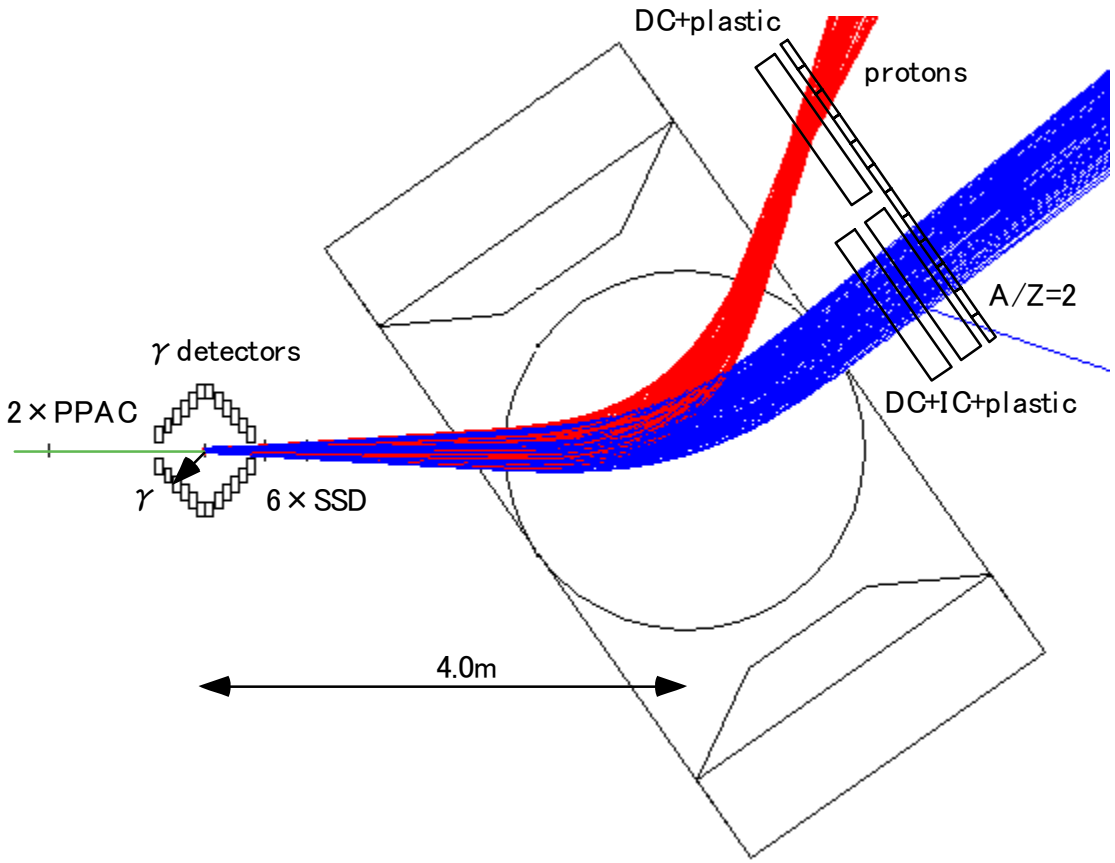

Fig. 2-4-4: Schematic view of the experimental setup for exclusive measurement mode. Trajectories were calculated in the same way as Fig.2-4-1.

The demerit of this setup compared to the above high resolution mode is the poorer resolution, as apparent from the smaller bending angle for reaction residues. In a Monte Carlo simulation, this setup is

not capable of separating the reaction residues of A>30 in 5σ, but the setup is applicable for light nuclei of A<30.

The detector lineup is almost the same as the high resolution mode. The angles of the protons and reaction residues are measured by two stacks of silicon telescopes which are apart by 150 mm. Reaction residues are also detected after the magnet by the a honeycomb cell drift chamber for position measurement, an ion chamber for energy loss measurement, and a plastic scintillator wall for TOF measurement. Protons are detected by a honeycomb cell drift chamber and a plastic scintillator wall for position and TOF measurement, respectively.

Figure 2-4-5 shows angular acceptance of protons and heavy ions. As one can see, the acceptance is better than the high resolution mode. Only slight event loss for protons is found. In Fig. 2-4-6, the simulated positions of protons and A/Z = 2 particles are shown. The horizontal and vertical directions of protons are roughly focused and defocused, respectively, while both horizontal and vertical directions of A/Z = 2 particles are defocused. The size of the detectors required are 1×0.8 m^2, and 1.2×0.8 m^2 for proton and A/Z = 2 particles.

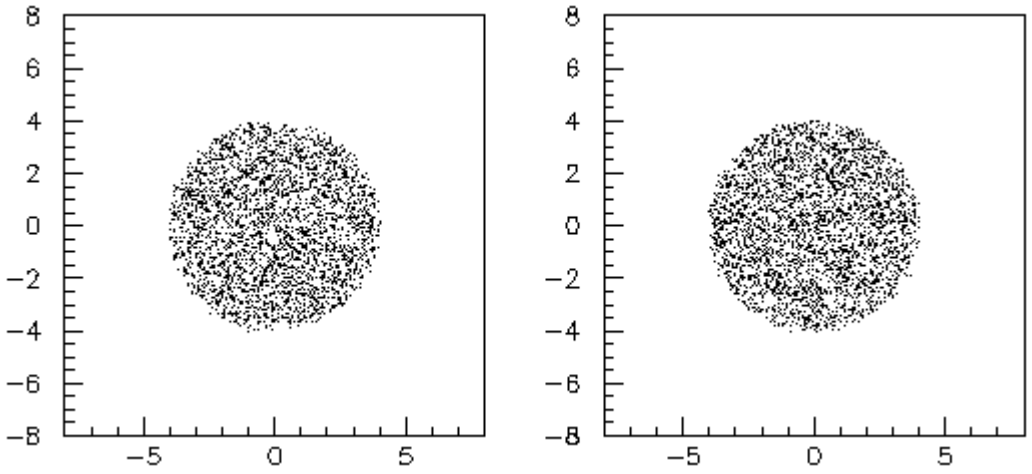

Proton A/Z = 2

Fig. 2-4-5: Angular acceptance of protons and A/Z = 2 particles in degrees in the vertical and horizontal directions calculated by Monte Carlo simulations using GEANT-3. The vertical and horizontal angular correlation of reaction products was plotted in coincidence with the focal plane detectors. Proton and A/Z = 2 beams were produced to fill uniformly in θ=0-4 degrees and ϕ=0-2π. For A/Z = 2 particles, no event loss is expected. For protons, only slight events are lost by hitting the yoke.

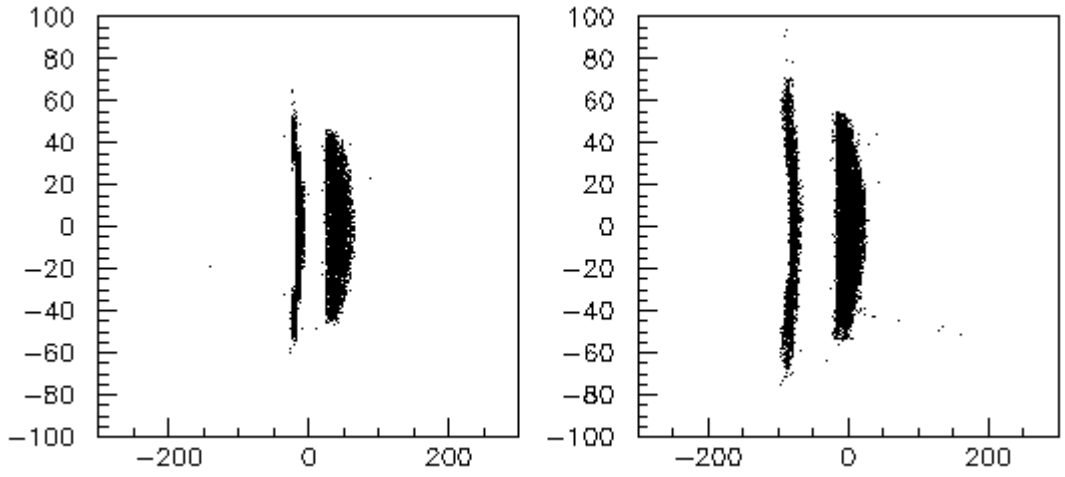

At drift chamber behind of plastic scintillator wall

Fig. 2-4-6: Position distribution on the focal plane detectors in cm calculated by Monte Carlo simulations using GEANT-3. Proton and A/Z = 2 particles at 250 *A* MeV were generated at the target to fill uniformly in θ = 0-4 degrees and ϕ = 0-2π.

[2-4-5] Other experimental devices

[2-4-5-1] RF deflector

This device is related to the impurities in the proton-rich RI beams produced in the projectile fragmentation reaction. In the proton-rich RI beams it is common that isotones close to the stability line are mixed. When a proton-rich isotope far from the stability is studied, the RI beam is almost governed by such impurities by, for instance, more than 99%. This situation is quite inefficient, since only less than one percent of the highest possible bean rate acceptable for the detectors available for the primary study. RF deflector works as a time-of-flight filter of the beam in the beam line, and hence purifies the beam. We propose to install this RF deflector at the tagging section of Big RIPS. Similar device is under operation at the RARF-RIPS facility and purity of secondary beam is successfully improved by a factor of 4 to 10.

[2-4-5-2] Gamma detectors

Breakup products may be in its excited states. In order to measure a decay of A→B*+p→B+p+γ, we place gamma-ray detectors around the target. For reaction cross section measurements where both of the ground state and bound excited state are possible to be the final state of the reaction, gamma ray detection may be indispensable. For gamma ray detection, we plan to use DALI-II NaI scintillator array and/or GRAPE Germanium detector array. Both of them are under operation in the current RIPS beamline.

[2-4-6] Cost estimation unit in KYen

• (RF deflector)	sub total:	(～100,000)
• Scattering angle measurement: silicon microstrip detector	sub total	15,800
• Silicon detector design (6 detectors)		5,000
• electronics		10,000
• temperature control system for front-end amplifier		800
• Momentum measurement for heavy ions:	sub total	0
Drift chamber proposed in [2-2-1] is usable.		
• Momentum measurement for protons:	sub total	35,000
• drift chamber including electronics		30,000
• 40 plastic scintillators + HV, QDC, TDC, etc.		5,000
• Gamma detectors:	sub total	0
• Total:		50,800
		(RF deflector: +～100,000)

[2-4-7] Manpower

Iwasa (Tohoku), Sümmerer (GSI), Bishop, Gomi, Motobayashi, Takeuchi, Yamada, Yoneda (RIKEN), 2-3 graduate students (Tohoku, Rikkyo etc.)

It would be helpful if RIKEN hires professional staffs for gas detectors and electronics.

[2-5] Detector system for polarized-deutron-induced reactions

[2-5-1] Experiments with polarized deuteron beams

We are planning the following measurements with polarized deuteron beams of E_d < 880MeV (440 MeV/A) at the SAMURAI spectrometer.

1) cross section and analyzing power measurements for *dp* scattering

2) cross section and analyzing power measurements for *dp* radiative capture reaction

3) spin correlation coefficient measurements for ^{3}He(*d*,*p*)^{4}He reaction

Goals of this measurement as well as the measurement 2) are to clarify the three nucleon force (3NF) effects quantitatively by direct comparison between the precisely obtained data and the exact solutions of three-nucleon Faddeev equations with modern NN forces. Recently the Faddeev calculations have predicted that large three nucleon force effects are clearly seen in the cross sections for elastic *dp* scattering, especially at backward angular region and they become larger as incident energy increases (see. Fig.2-5-1). Also the relativistic effects are predicted to be larger at higher energies.

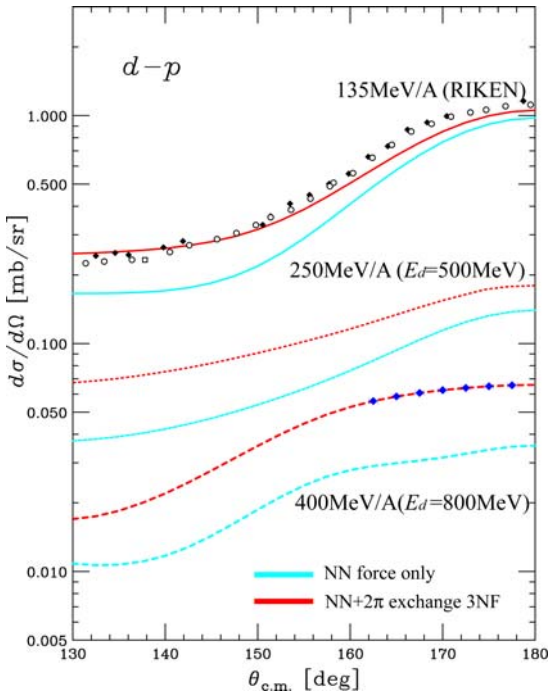

Figure 2-5-1. Differential cross sections for elastic *dp* scattering at 135MeV/A, 250MeV/A, and 400 MeV/A. The blue lines are the Faddeev calculations based on the AV18 NN potential. The Faddeev calculations including 2π-exchange 3NF are shown with the red lines.

Thus we will focus on the precise measurements at backward angles ($\theta_{c.m.}$ = 160°－180°) using the SAMURAI spectrometer covering the wide energy range of 250 MeV/A – 440 MeV/A. In the experiments the polarized deuteron beams with an intensity of 1pnA bombard a polyethylene (CH_2) solid target. Note the beam intensity of deuteron beams is limited to 1pnA due to the regulation for radiation. The scattered protons are momentum analyzed by the SAMURAI spectrometer and detected at the focal plane. The expected focal plane detectors are a multi-wire drift chamber and plastic scintillators. The drift chamber is used for the reconstruction of the trajectories of the scattered particles and the hodoscope is used for particle identification. The main backgrounds are considered to be deuterons from inelastic scattering on ^{12}C and also protons produced in the deuteron breakup process. The background deuterons are eliminated by the light outputs of plastic scintillators. To estimate the proton background events the

excitation energy spectra for the measurement at 135 MeV/A are shown in Fig.2-5-2 as a reference. As the figure shows the energy resolution δE ～1MeV is required at least in order to resolve the energy spectra of the elastic events and the breakup events, which corresponds to the momentum resolution $p/\delta p$ ～1600 for 1.5 GeV/c proton. A good angular resolution is also necessary for direct comparison between the data and the state-of-the-art Faddeev calculations and nailing down the angular dependence of 3NF effects quantitatively. If the angular resolution is ～0.5°, the data are obtained with the angular bin ～2° in the center of mass system. The expected results of the cross sections at 400MeV/A are shown with the blue diamonds in Fig. 2-5-1. To extract the cross section, it is also essential to obtain the number of the deuteron beams, which are extracted by collecting the beam charges in a beam dump. For the descriptions on a beam dump, see Sec. 2-5-2.

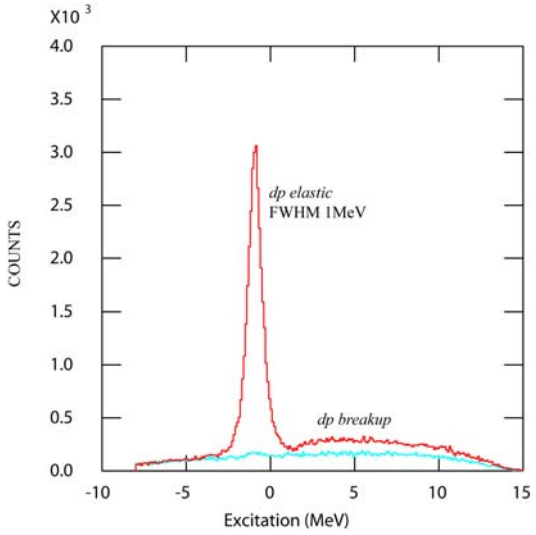

Figure 2-5-2. Excitation energy spectra for elastic dp scattering at 135 MeV/A.

2) cross section and analyzing power measurements for $dp \rightarrow {}^3\mathrm{He}$ radiative capture reaction

For this reaction, the angular range of interest is $\theta_{\mathrm{c.m.}}(d \rightarrow {}^3\mathrm{He})=130° - 180°$ which corresponds to the angles $\theta_{\mathrm{lab.}}(d \rightarrow {}^3\mathrm{He}) = 0° - 7°$ in the laboratory system to study the three nucleon force and meson-exchange currents. Then we will measure focusing on this angular region. The predicted cross section of the radiative capture reaction is small (10nb/sr) and then the liquid hydrogen target is used to reduce the background proton events in the deuteron breakup process as is shown in *pd* elastic scattering. The film of the target cell easily swells when the liquid hydrogen is contained. Therefore the effective target thickness is estimated by measuring the cross section of *dp* elastic scattering. The scattered ${}^3\mathrm{He}$ are detected at the focal plane. The backgrounds are considered to be protons in the deuteron breakup process, deuterons from inelastically scattering on ${}^3\mathrm{He}$ and/or target cell and ${}^3\mathrm{He}$ from ${}^1\mathrm{H}(d, {}^3\mathrm{He})\pi_0$ reactions. The background protons and deuterons are eliminated by the light outputs of plastic scintillators and the time of flight (TOF) information. As a reference, Fig.2-5-3 shows the spectra of scintillator detector light output at the focal plane together with the spectra where the energy outputs and TOF gates were applied for the measurement at 135 MeV/A .

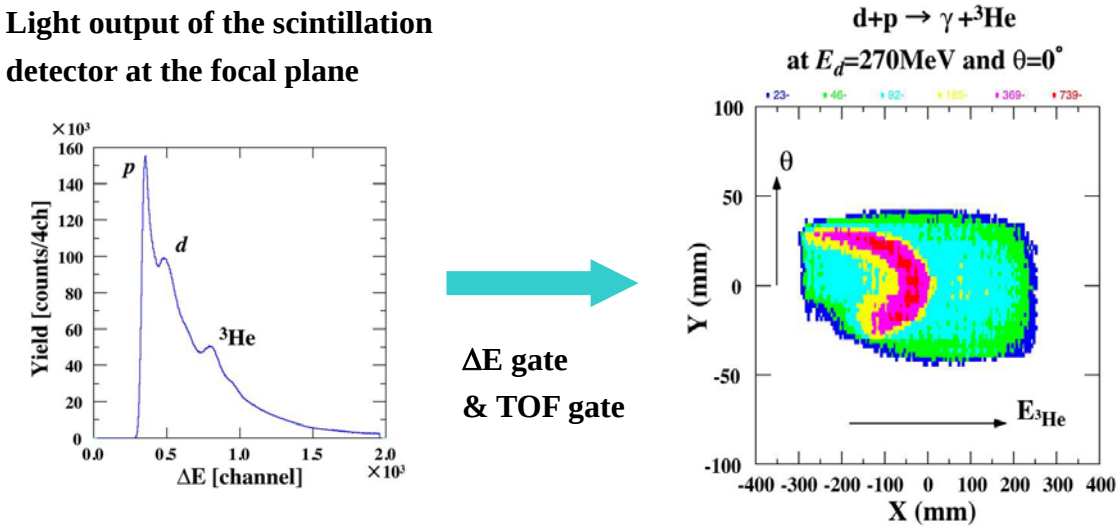

Figure 2-5-3. spectra of scintillator detector light output at the focal plane for *dp* radiative capture measurement at 135 MeV/A and the spectra of focal plane positions corresponds to the energy and angles.

The background ^{3}He from ^{1}H(d, ^{3}He)π_0 are easily resolved due to the momentum difference and the momentum resolution of the SAMURAI dipole magnet $p/\delta p$=600～700 is enough to resolve (See Fig.2-5-4). Figure 2-5-4 shows the relation between the scattering angles of ^{3}He in the laboratory system and those in the center of mass system. If the angular resolution is 0.5 ° , the data are obtained with the angular bin 1.5－3° in the center of mass system, which is mostly acceptable for comparison with Faddeev calculations.

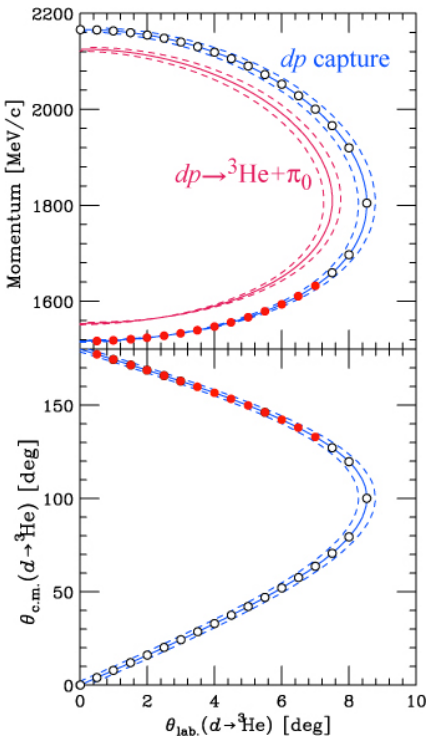

Figure 2-5-4. Kinematics of the $dp \rightarrow {}^3\mathrm{He}+\pi_0$ reaction and *dp* radiative capture reaction. Upper panel shows the relation between the scattering angles of ^{3}He in the laboratory system and the momentum for *dp* radiative capture and ^{1}H(d,^{3}He)π_0 reactions. The lower panel shows the relation between the scattering angles of ^{3}He in the laboratory system and those in the center of mass system. The dashed lines reflect the angular resolution $\delta\theta$=0.5° in the laboratory system. The angles of interest are shown with red solid circles.

3) Spin correlation coefficient measurements for ^{3}He(d,p)^{4}He reaction

For this reaction, the angle of interest is $\theta_{c.m.}=0^\circ$ ($\theta_{lab.}=0^\circ$). The polarized deuteron beams bombard the polarized ^{3}He gas target and the scattered protons are detected at the focal plane. The main backgrounds of this reaction are the protons from the deuteron breakup reactions of d+^{3}He→pn3He, d+^{16}O→pn^{16}O, and d+^{28}Si→pn^{28}Si. Oxygen and silicon are the materials of the target cell. Figure2-5-5 shows the predicted energy spectra with the momentum resolutions $p/\delta p$=300 and 1000 at E_d=1GeV (E/A=500MeV). As is shown in the figure, the high momentum resolution $p/\delta p$=1000 is required to subtract background contributions and extract the events of ^{3}He(d,p)^{4}He reaction. The solid angle is determined by the double slits installed in the scattering chamber.

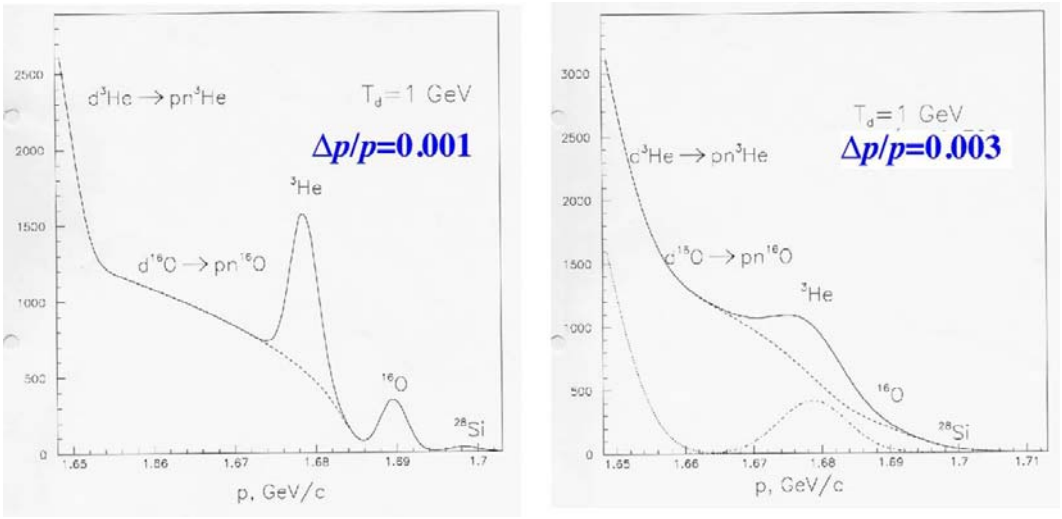

Figure 2-5-5. Predicted energy spectra for the experiments ^{3}He(d,p)^{4}He reaction at the focal plane when the momentum resolutions $p/\delta p$=300 and 1000 at E_d=1GeV (E/A=500MeV).

Experimental conditions for each measurement are summarized in Table 2-5-1.

Reaction	***dp* elastic scattering**	***dp*→ ^{3}He +γ**	**^{3}He(*d* ,*p*)^{4}He**
Measured Observables	**$d\sigma/d\Omega$, Analyzing powers**	**$d\sigma/d\Omega$, Analyzing Powers**	**Spin correlations coefficients**
$d\sigma/d\Omega$(c.m.)	**～50μb/sr**	**～10nb/sr**	**～5μb/sr**
Angular Range ($\theta_{c.m.}$)	**160° － 180°**	**130° －180°**	**0° －1.6°**
Angular Range ($\theta_{lab.}$)	**0° －5°**	**0° －7°**	**0° －1°**
Beam	**880 MeV (2.0 GeV/c) Polarized Deuterons**		
Target	**CH_2 (3mm^t)**	**Liq. Hydrogen (5mm^t)**	**Polarized ^{3}He gas target**
Detected Particles (DP)	**proton**	**^{3}He**	**proton**
Kinetic Energy of DP	**800 MeV**	**380 MeV ～440 MeV**	**870 MeV**
Momentum of DP	**～1.5 GeV/c**	**1.5 GeV/c ～1.6 GeV/c**	**～1.6 GeV/c**
Momentum Ratio : P_{beam} / [P (DP)/Q]	**～1.4**	**2.4 ～2.7**	**～1.3**
Momentum Resolution $p/\delta p$	**1600**	**600**	**1000**
Angular Resolution ($d\theta_{lab.}$)	**0.5°**	**0.5°**	**0.5°**

Table 2-5-1. Experimental conditions using polarized deuteron beams at SAMURAI spectrometer

[2-5-2] High resolution option with triplet Q-magnets and experimental apparatus

In experiments where high momentum resolution of $p/\delta p \sim 1600$ is required, triplet Q-magnets of the beam-line are used for momentum analysis of scattered particles in conjunction with the SAMURAI spectrometer (the Q3D mode). Expected performances of the Q3D mode are,

Dispersion 2.25 m ,
Magnification (x|x) = 0.5, (y|y) = −15.7,
Vertical angular acceptance ＋/－90mrad
Horizontal angular acceptance ＋/－60mrad
$p/\delta p$ ～ 3000 .

The calculations were performed using the OPTRACE code with a realistically calculated magnetic field of the dipole magnet. The matrix elements are shown in Table 2-5-2. Scattered particles are momentum-analyzed in Q3D and detected with the focal plane detector of SAMURAI. Figure 2-5-6 shows the schematic view of the experimental setup for the Q3D mode measurements. The expected detectors are a multi-wire drift chamber (MWDC) and plastic scintillator hodoscope located 3 m downstream from the center of the SAMURAI dipole magnet. To cover the momentum byte Δp/p = 8% maintaining the momentum resolution $p/\delta p$ ～3000, and the angular resolution $\delta\theta$(h,v) ～0.5° the focal plane detectors are required to cover the region 70cm^{W}×120cm^{H}. The specifications of MWDC and the hodoscope are summarized in Table 2-5-3.

As Table 2-5-1 shows, the momentum ratio P(*d* beam)/(P(detected particle)/Q) varies from 1.3 to 2.7 depending on the measured reactions. When we change the momentum region of the detected particles, we change the magnetic field and move a beam dump correspondingly in order to maintain the good resolution at the focal plane detector.

For the beam charge collection we install a beam dump 6m downstream of the center of the SAMURAI dipole magnet to stop 880MeV deuteron beams which consists of a Fe block (40cm in length). To reduce the emitted neutrons when the beams stop, the beam dump is shielded with concrete blocks of volume 72 m^3 (4.0m^{D}×4.5m^{W}×4m^{H}) in total. As mentioned before, the beam dump is required to be a movable and rotary one. The open geometry of the SAMURAI makes it possible to place and move such a large beam dump. The schematic view of SAMURAI in Q3D mode are shown in Fig. 2-5-6 .

$$\begin{pmatrix} (x|x) & (x|a) & (x|y) & (x|b) & (x|z) & (x|\delta) \\ (a|x) & (a|a) & (a|y) & (a|b) & (a|z) & (a|\delta) \\ (y|x) & (y|a) & (y|y) & (y|b) & (y|z) & (y|\delta) \\ (b|x) & (b|a) & (b|y) & (b|b) & (b|z) & (b|\delta) \\ (z|x) & (z|a) & (z|y) & (z|b) & (z|z) & (z|\delta) \\ (\delta|x) & (\delta|a) & (\delta|y) & (\delta|b) & (\delta|z) & (\delta|\delta) \end{pmatrix} = \begin{pmatrix} -0.47453 & -0.00086 & 0.00000 & 0.00000 & 0.00000 & 2.24623 \\ -10.19382 & -2.09763 & 0.00000 & 0.00000 & 0.00000 & 8.12441 \\ 0.00000 & 0.00000 & -15.66871 & -0.37668 & 0.00000 & 0.00000 \\ 0.00000 & 0.00000 & -22.70156 & -0.60993 & 0.00000 & 0.00000 \\ 0.00000 & 0.00000 & 0.00000 & 0.00000 & 1.00000 & 0.00000 \\ 0.00000 & 0.00000 & 0.00000 & 0.00000 & 0.00000 & 1.00000 \end{pmatrix}$$

Table 2-5-2. Matrix elements of the SAMURAI spectrometer in Q3D mode. The units of x, a, y, b, and δ are cm, mrad, cm, mrad and %, respectively.

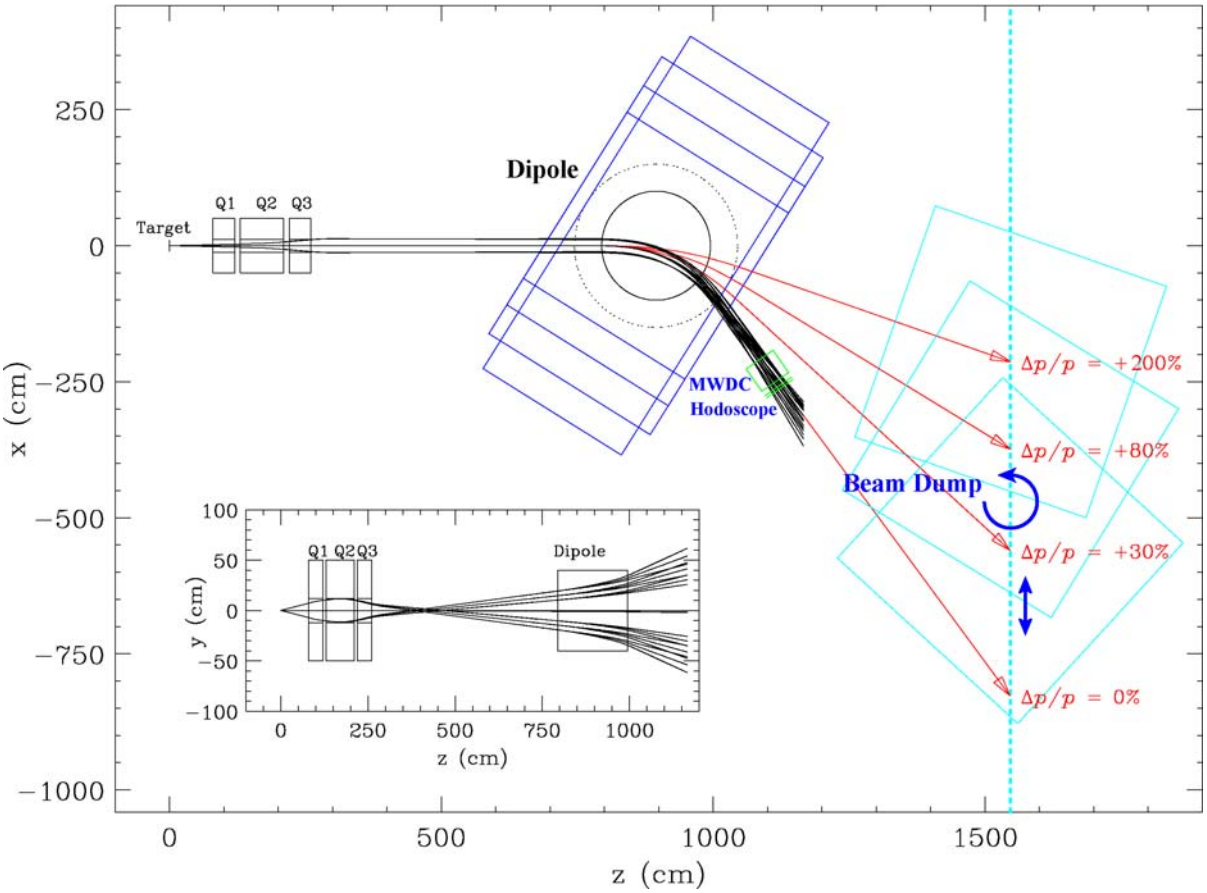

Figure 2-5-6. Schematic view of the SAMURAI spectrometer in Q3D mode

MWDC	**X-plane**	**Y-plane**
Total Volume	**70cm^{W}×140cm^{H}×50cm^{D}**	
Number of Planes	**8(X-Y-X'-Y'-X'Y'-X-Y)**	
Sensitive Area	**64cm×128cm**	
Separation of XY planes	**20mm× 20mm**	**20mm×20mm**
Cell Size	**32 cells/plane**	**64 cells/plane**
Hodoscope		
Total Size / Layer	**70cm^{W}×120cm^{H}×1cm^{T}**	
Number of Layers	**2**	
Number of Plastic Scintillators /Layer	**8**	
Size of Plastic Scintillator	**70cm^{W}×120cm^{H}×1cm^{T}**	

Table 2-5-3. Specifications of the focal plane detectors.

For the polarized deuteron beam measurements, the following additional beam line and devices are

necessary.

1) a beam line which connects directly between the RRC and SRC but skips the IRC.
2) beam monitoring devices for light ions (Z＝1) at Big RIPS

   The expected beam tuning devices are fiber scintillators or multi-wire drift chambers. They should be installed at each focal plane of Big RIPS (F1-F9).
3) a beam line polarimeter which should be installed downstream of SRC
4) a beam line polarimeter which should be installed on the beam line which directly connects the RRC and SRC

   For this polarimeter, we modify the present beam line polarimeter installed in the beam distribution room (D-room) of the RARF.

[2-5-3] Upgrade of focal plane detector system at SAMURAI

We will extend the focal plane detector system at SAMURAI to the focal plane proton and/or deuteron polarimeter which is used for polarization transfer coefficients of nuclear reactions, e.g. deuteron to proton polarization transfer coefficient measurement for *d-p* elastic scattering. For the construction of the focal plane polarimeter, one needs

a. additional developments of multi-wire drift chamber and hodoscope system
b. study of proton and/or deuteron beam operation
c. calibration of the focal plane polarimeter

[2-5-4] SCHEDULE

FY2006

Detector design studies and R&Ds

FY2007

a. construction of beam tuning devices [2 people]
b. construction of beam line polarimeter : detector & target system [2 people]
c. construction and installation of beam dump at SAMURAI [2 people]
d. polarized deuteron beam acceleration at RIBF
e. calibration of deuteron beam-line polarimeter
f. *dp* elastic measurements with beam line polarimeter system
g. construction of the scattering chamber & target system for SAMURAI Q3D-mode [2 people]

FY2008

a. *dp* breakup measurements with beam line polarimeter
b. construction of detector systems at SAMURAI [3 people]

FY2009

a. experiments at SAMURAI with polarized deuteron beams
   - ^{3}He(*d*,*p*)^{4}He reaction
   - *d*+*p* radiative capture reaction

- *dp* elastic scattering at backward angles

b. construction of focal plane polarimeter system at SAMURAI (upgrade) [3 people]

[2-5-5] COSTS

1. Detectors at SAMURAI
   a. MWDC (X : 128ch, Y : 256ch) : 10 MYen
   b. Hodoscope (Plastic scintillators and Photo-multipliers) :
      300,000 Yen × 16 = 4.8 M Yen
   c. Holder : 5 M yen
   d. Electronics :
      - TDC for MWDC (AMSC 64ch/module TDC) 8 modules
        340,000 Yen/module × 8 = 2,620 kYen
      - Pre Amplifier Card (REPIC 16ch /card) 30 cards
        30,000 Yen/card × 30 = 900 kYen

2. Beam monitoring devices for light ions (Z=1) at Big RIPS : 7 M Yen
3. Beam dump at SAMURAI : 25 MYen
4. Scattering chamber and target system at SAMURAI in Q3D mode : 3 MYen
5. Beam Line Polarimeter downstream of SRC : 5 M yen

[2-5-6] UNIQUENESS

Polarized deuteron beams with energies of > 500MeV can be accelerated at Nuclotron of JINR and very recently at COSY. However, they have a polarization only in vertical direction (y-axis). The polarized deuteron apparatus at RIKEN is very unique in its spin-direction control. It can provide a polarized beam with deuteron polarization directed in *any* direction.

[2-5-7] EXPERIMENTAL EXAMPLE

1) Analyzing power and polarization transfer measurement for the *dp* scattering, and radiative capture reaction.
2) Polarization correlation measurement for the ^{3}He($\vec{d}$,$\vec{p}$)^{4}He reaction

[2-6] SAMURAI TPC (Technical Consideration)

[2-6-1] Introduction

In order to study the density dependence of the asymmetry term of the EOS we should measure π^+ and π^- yield ratios at a variety of impact parameters and for a variety of colliding systems with different total isospin. In the following, we discuss technical issues relevant to the construction of a SAMURAI TPC to probe the density dependence of the EOS asymmetry term. The discussion of design considerations draws considerably from experiences with the EOS TPC.

Measurements of the density dependence of the asymmetry term using a SAMURAI TPC require the SAMURAI magnet, the SAMURAI TPC, beam tracking detectors, a fast trigger detector array, and the associated electronics. In the next section, we discuss the technical requirements for the various components. This is followed by a discussion of the required R&D, manpower, budget, and timetable for construction of the array.

[2-6-2] Requirements for the SAMURAI magnet.

The proposed SAMURAI dipole magnet has a pole diameter of 2 m and a pole gap of 0.8 m. It is comparable to the 2.1 m diameter and 1.0 m pole gap of the HISS dipole used at the BEVALAC. The magnetic volume is adequate to house a rectangular TPC with approximate length of 1.5 m, width of 1 m and height of 0.6 m. The dimension of the SAMURAI TPC would be similar to the 1.5 x 0.95 x 0.75 m^3 dimensions of the EOS TPC. The exact vertical dimension of the SAMURAI TPC depend on details of the electrode and readout structures of the TPC that have not been decided at the present time.

To ensure tracking in the TPC, an accurate field map of the inner volume (within a diameter of 1.m at the center of the magnet) will be needed before accurate momentum measurements are performed. If the TPC operates at atmospheric pressure the optimal field for the TPC will 1.5 T or less. (E x B drift velocity effects degrade the performance of the TPC at higher magnetic fields.)

The existing data of π^- energy spectra for ^{139}La+^{139}La reaction indicate that p_T of πs from Sn+Sn reaction around 350 MeV/A would be as large as 420 MeV/c. With the above-mentioned configuration of the SAMURAI TPC we could cover such a transverse momentum domain around rapidity region of 0.42, which corresponds to a mid-rapidity, $(y_p+y_T)/2$.

[2-6-3] Requirements for the SAMURAI TPC

The SAMUARI TPC must accurately measure minimum ionizing p, π^+ and π^- in the presence of a projectile-like residue and a large multiplicity of intermediate mass fragments (IMF's). This requires slight reduction of gas amplifications for heavier, more strongly ionizing particles, which can be achieved by using wire anodes of different radius or by running the anode wires at different voltages. In the EOS TPC, different gas gains were achieved by the latter technique. Figure 2-6-1 shows the arrangement between anode wires and the readout pads used for the EOS TPC. An associated charged-particle multiplicity for the Sn+Sn reactions around 350 MeV/A is expected to be as large as 80 therefore we estimated a two-track resolution of TPC should be better than 3.6 cm. The EOS TPC had 15360 pads of 12mm x 8mm. These

pad dimensions set the scale for the 2.5 cm two-track resolution of the EOS TPC. Similar pad dimensions would provide us a desired resolution.

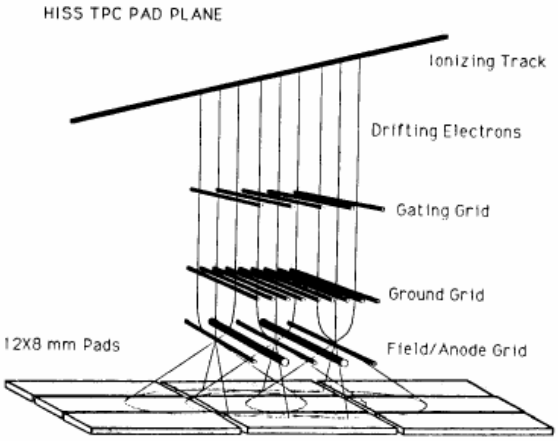

Figure 2-6-1: HISS TPC Wire and Pad Plane layout

The π^+ and π^- yields must be measured with a relative accuracy of about 1%. This presents a challenge because negative pions can be readily distinguished from positively charged particles by the opposite curvature of their tracks, while the tracks of positive pions must be measured at a sufficient number of points so that they can be distinguished from protons by their ionization density. Figure 2-6-2 shows the results of a simulation for events at E/A=400 MeV, assuming a TPC performance equivalent to that of the STAR TPC. In this case, positive pions can be clearly distinguished from protons. (It should be noted that the measured performance of the EOS TPC was similar, but slightly poorer.) The pad dimensions for the STAR TPC were 2.85 mm x 11.5 mm for the inner sectors and 6.20 mm x 19.5 mm for the outer sectors

Design studies for the STAR TPC indicated that the track and PID resolutions of the TPC were a gradual function of the number of pads. For the SAMURAI TPC, one should vary the pad dimensions with larger pads at backward angles where the track density will be less and smaller pads at forward angles near the beam. It should be possible to build a device with 15000 pads; superior results would be obtained if one increases the number of pads to 30000. That is the number used in the budget estimate below.

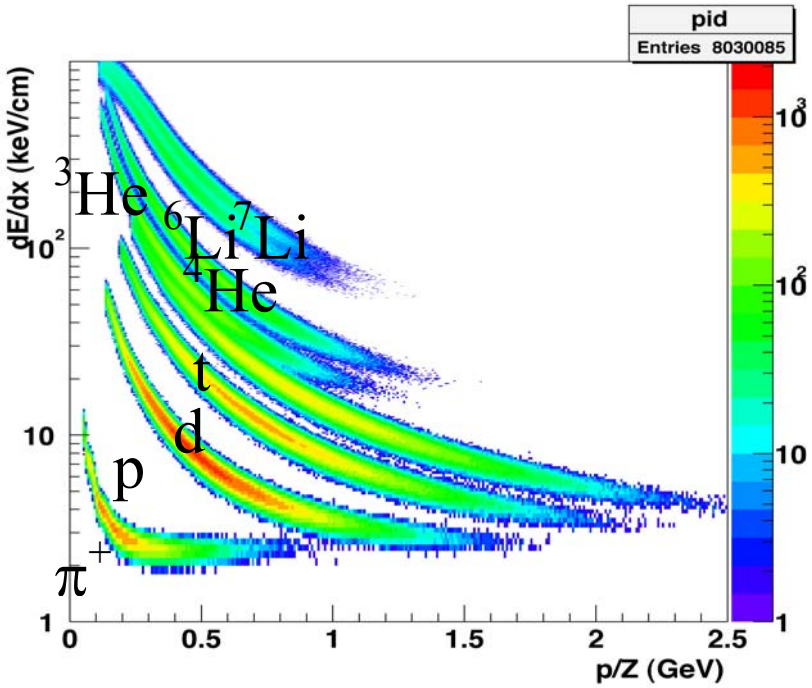

Figure 2-6-2: Simulate PID for SAMURAI TPC, assuming a performance similar to the STAR TPC.

[2-6-4] Requirements for the trigger

The SAMURAI TPC requires a fast trigger. This can be provided by an array of plastic scintillators arranged outside of the TPC volume at forward angles $\theta<60^{o}$. Placing the array just outside the volume minimizes costs; placing it farther away increases the cost and the capability of the array for particle identification. Time of flight resolution can be optimized by the use of a diamond start detector, which would provide a start signal with a 10 picoseconds timing resolution.

[2-6-5] Required R&D:

The operating parameters of the TPC lie within the ranges of existing devices. Major uncertainties primarily concern the mechanics of the TPC vessel and how the mechanical design of the TPC vessel and pad layout influences the detector performance. To test these issues, one could build a test TPC.

[2-6-6] Required manpower

The mechanical design of the TPC would require about 1 man-month of design time, spread out over 6 months. Construction of the TPC vessel would require about 6 man months spread out over 1.5 years.

The electronics for the TPC should be adapted from one of the large TPC projects, such as the Alice TPC at CERN by paying for extension of a chip production run. Many extra channels were produced for the STAR TPC. STAR readout electronics has been extensively used at the NSCL of MSU and at other laboratories, but this source of readout electronics is now pretty much exhausted. Building the chip electronics into a complete readout system requires little R&D, but would require the services of an electronics engineer for about 1 man years spread out over two years. We hope to get some help from the NSCL electronics shop for the R&D.

In total we estimate that a team of about 4 PhD. level physicists working 50% of their time on this project for about 4 years would be able to bring it to completion.

[2-6-7] Budget

Table provides an estimate of the equipment cost for the TPC in dollars. It is a rough estimate and is based on the cost when we make the entire TPC in USA, which would be nearly a factor of 2-3 cheaper than the one required in Japan. The estimation should be, any way, redone before submission of a funding proposal.

Cost Estimates for TPC			
Item	*Unit cost (k$)*	*# units*	*cost (k$)*
TPC detector w/out electronics	75.000	1	75.0
TPC electronics	395.800	1	395.8
Laser, HV, misc.	66.000	1	66.0
Chamber	100.000	1	100.0
Gas handling system	1.500	1	1.5
Plastic scintillator trigger	60.000	1	60.0
Total			698.3

In order to reduce the total cost we have also considered an option of renting the existing EOS TPC. Since the EOS TPC requires a 1 m gap its chamber need to be modified considerably. Making a new TPC chamber that is a copy of the EOS TPC but is less tall could be more easily done. Its electronics is twenty years old and is obsolete, and the computer acquisition is obsolete as well. We judge, therefore, it is not realistic to reuse the EOS TPC for the SAMURAI.

[2-6-8] Further Extension

Calculations indicate that the comparison of neutron and proton transverse flows and momentum distributions can provide additional constraints on the density dependence of the asymmetry term at supra-normal densities. To investigate these observables, it would be useful to have an efficient neutron detector. The detector proposed in **[2-3]** in this proposal is suitable for this purpose.

The flexibility and power of a TPC would be enhanced by the availability of a detector, such as at TP-MUSIC, at forward angles that is designed to measure the projectile-like residue.

In Fig. 2-6-3, we provide a schematic drawing of a setup that includes all of these components.

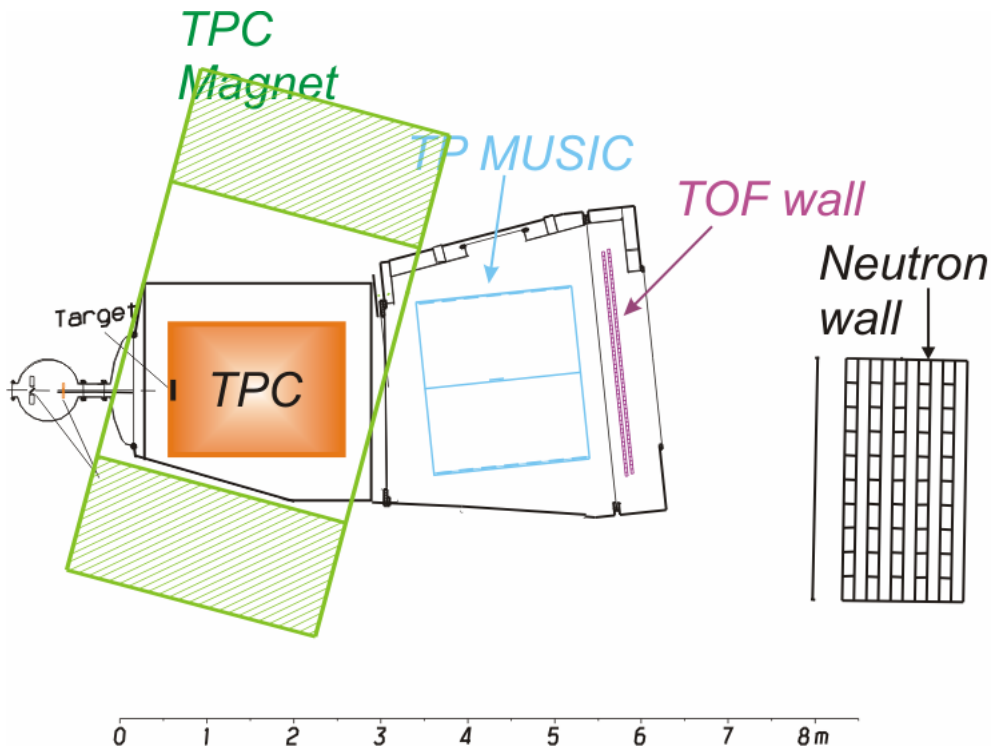

Figure 2-6-3: Schematic layout of an experiment with the TPC. This drawing does not yet reflect the shape of the SAMURAI magnet nor the space constraints.

[3] Summary of cost, schedule, and manpower

In table 3-1, costs, schedule, and manpower timetables are summarized. For the present plan, the magnet proposed in [2-1], gas chambers and PID detectors proposed in [2-2], and neutron detectors proposed in [2-3], are to be ready with highest priority in 2008. The (γ,p) type experiments and polarized deuteron induced experiments are also important and are prepared to be ready in 2009. The SAMURAI TPC project is a relatively long term plan requiring 4 years to be ready. For the costs here, design studies, R&Ds, and running costs are supposed to be covered by other budgets, and only construction costs are listed.

Schedule	FY2006	FY2007	FY2008	FY2009	FY2010
SAMURAI Magnet [2-1]	Design	Construction Test	Operation		
Drift Chambers [2-2-1]	R&D Design	Construction Test	Operation		
PID Detectors [2-2-2]	R&D Design	Construction Test	Operation		
Neutron Detectors [2-3]	R&D Design	Construction Test	Operation		
(g,p) Exp. [2-4]	R&D Design	Construction Test	Operation		
Pol. Deuteron Exp. [2-5]	R&D Design	Construction Test	Operation		
SAMURAI TPC [2-6]	R&D Design	TPC Construction	Electronics	Operation	

Manpower Cost [MYen]	FY2006	FY2007	FY2008	FY2009	FY2010	Total
SAMURAI Magnet [2-1]		RIKEN Accelerator Group				
		500.	500.			1,000.
Drift Chambers [2-2-1]	2 persons + 1 prof. staff	2 persons + 1 prof. staff	2 persons + 1 prof. staff	2 persons + 1 prof. staff	2 persons + 1 prof. staff	
		29.4	46.1			75.5
PID Detectors [2-2-2]	2 persons + 1 prof. staff	2 persons + 1 prof. staff	2 persons + 1 prof. staff	2 persons + 1 prof. staff	2 persons + 1 prof. staff	
		2.4	9.0			11.4
Neutron Detectors [2-3]	2 persons	2 persons + 1 prof. staff	2 persons + 1 prof. staff	2 persons + 1 prof. staff	2 persons + 1 prof. staff	
		20.	190.			210.
(g,p) Exp. [2-4]	2 persons	2 persons	2 persons + 1 prof. staff	2 persons + 1 prof. staff	2 persons + 1 prof. staff	
			20.8	30.		50.8
Pol. Deuteron Exp. [2-5]	2 persons	2 persons	3 persons	3 persons	3 persons	
		40.	23.3			63.3
SAMURAI TPC [2-6]		2 persons	2 persons	2 persons + 1 prof. staff	2 persons + 1 prof. staff	
		10.	20.	15.	25.	70.
		(TPC costs are assuming collaboration with a forein institute)				
Total Cost		601.8	809.2	45.	25.	1,481.

Table 3-1 Summary of schedule, cost, and manpower.